Norges miljø- og
biovitenskapelige
universitet

Master's Thesis 2017 30 ECTS
Faculty of Science and Technology

First order magnetostructural transitions in the Fe-doped MnNiGe magnetic equiatomic compound

Marius Kristiansen
Environmental physics and renewable energy

Preface

As I entered the field of energy physics at the Norwegian University of Life Science, energy production, storage, and consumption caught my interest. In addition to general interest of the subjects, the opportunity to work with new innovative technologies contributing to a sustainable development of the future motivated me. Energy physics was thereby a natural choice of subject for my master thesis. During my fourth year at the university, I contacted The Physics Department at IFE by recommendations from Arne Auen Grimenes. IFE presented a few interesting research proposals, including the field of solid-state refrigeration, which is the subject of this work.

Today I am grateful for having had the pleasure to learn form and work with the skillful and experienced people at IFE. The learning curve has been steep, but the experience although more exciting.

I would like to thank my supervisors Bjørn Christian Hauback and Arne Auen Grimenes for skillful guidance and feedback during the last four months and I would like to give a special thanks to Christoph Frommen, for many hours of proficient lab work training, data analysis guidance and feedback.

I would also like to thank Magnus Helgerud Sørby for lab training, helping with the neutron diffraction experiment and teaching me the Rietveld refinement technique. In addition I would like to thank Santosh Kumar Pal and Marion Jeanne Louise Duparc for helping with magnetic measurements and Antonin Cajka for helping me with scanning electron microscopy at UIO.

Finally, I would like to thank my friends, family and girlfriend for motivation, support and good times through these five years of study.

Ås, May 12th, 2017

Marius Kristiansen

Sammendrag

Magnetisks kjøleteknologi basert på den magnetokaloriske effekt er en miljøvennlig og teknologi med høy virkningsgrad. Teknologien har et stort potensiale og kan i fremtiden vise seg å være en fornuftig erstatning av tradisjonell, mindre effektiv gass-kompresjons kjøleteknologi [1]. En signifikant magnetokalorisk effekt har blitt rapportert i materialer som gjennomgår en magnetostrukturell faseovergang [2].

Målet med denne oppgaven er å etablere en magnetostrukturell faseovergang i en MnNiGe legering med variert Fe-erstatning, og videre undersøke legeringens potensiale som et magnetisk kjølemateriale. Totalt elleve $Mn_{1-X}Fe_XNiGe$ og $MnNi_{1-X}Fe_XGe$ legeringer ble syntetisert og undersøkt.

Strukturelle endringer som en funksjon av Fe-erstatning ble påpekt ved bruk av røntgen og nøytron diffraksjon. Magnetiske faseoverganger ble undersøkt ved hjelp av et physical property measurement system. Termodynamiske egenskaper ble undersøkt for a å bestemme strukturelle faseovergangstemperaturer til prøvene. Disse egenskapene ble undersøkt ved hjelp av et kalorimeter. En analyse av prøvenes element-sammensetning ble utført ved hjelp av et elektronmikroskop.

MnNiGe legeringen viser seg å ha en primitiv orthorombisk krystallstruktur ved rom temperatur. Med tilstrekkelig Fe-erstatning av Mn eller Ni får legeringen en heksagonal krystallstruktur. Denne (diffusjonsløse martensittiske) transformasjonen forekommer også ved temperaturendring av materialet. Den strukturelle faseovergangstemperaturen reduseres markant ved høyere jerninnhold i prøven. Dette gjør det mulig å justere faseovergangstemperaturen mot romtemperatur, noe som er ønskelig hvis materialet skal brukes i et magnetisk kjøleskap. Magnetiske målinger påviser etablering av en magnetostrukturell faseovergang idet nok jern er introdusert i legeringen.

Både magnetiske og strukturelle faseoverganger viste hysterese. Dette er assosiert med effekttap ved bruk magnetisk kjøleteknologi. For $Mn_{0.85}Fe_{0.15}NiGe$ legeringen ble maksimum entropi endring under en magnetostrukturell faseovergang (trigget at et magnetisk felt på $\Delta H = 2\ T$) beregnet til $6.46\ \frac{J}{Kg*K}$. Legeringen viser seg å være en god kandidat som et magnetisk kjølemateriale.

Abstract

Solid state refrigeration based on the magnetocaloric effect is an efficient and environmental friendly cooling technology. It holds great promise as a futuristic replacement of the traditional, less efficient vapor compression technology [1]. A Giant magnetocaloric effect has been reported in materials undergoing a magnetostructural transition [2].

The aim of this master thesis is to establish a magnetostructural transition in the magnetic equiatomic MnNiGe alloy by Fe-substitution and investigate the intermetallic compound's potential as a magnetic refrigerant. A total of eleven $Mn_{1-x}Fe_xNiGe$ and $MnNi_{1-x}Fe_xGe$ samples were synthesized and characterized.

Structural changes as a function of elemental composition were determined using X-ray and neutron diffraction. Magnetic ordering temperatures were investigated by the physical property measurement system. Thermodynamic properties were investigated for determination of structural transitions temperatures of the samples. These properties were investigated by the use of differential scanning calorimetry. An analysis of compound's morphology and elemental composition was performed using a scanning electron microscope.

The MnNiGe compound forms a primitive orthorhombic crystal structure at room temperature. As a sufficient amount of Fe is substituted on the Mn or Ni site of the compound, the material forms a primitive hexagonal crystal structure. This diffusionless martensitic transformation is also triggered by sample temperature regulation. The structural transition-temperature of the samples is significantly reduced with higher Fe content. This makes the transition-temperature tunable towards room temperature, which is desired for magnetic refrigeration technologies. Magnetic measurements indicate the establishment of a magnetostructural transition with sufficient Fe-substitution.

Both the magnetic and structural transition indicated hysteresis, which is associated with effect loss in a magnetic heat pump device. The $Mn_{0.85}Fe_{0.15}NiGe$ shows a maximum entropy change of 6.46 $\frac{\mathrm{J}}{\mathrm{Kg}*\mathrm{K}}$ during a magnetostructural transition triggered by a magnetic field $\Delta H = 2$ T. The alloy appears to a good candidate magnetic refrigerant material.

List of symbols

Symbols	Description	Unit
T	Temperature	K and ℃
T_N	Neel temperature	K
T_C	Currie temperature	K
T_{hys}	Thermic hysteresis	K
x	Iron content	%
a, b, c	Lattice distance parameters	Å
α, β, γ	Lattice angle parameters	°
h, k, l	Miller indices	Dimensionless
θ	Radiation angle	°
d_{khl}	Atomic plane distance	Å
λ	Radiation wave length	Å
$\vec{\mu}$	Magnetic moment	Am^2
M	Magnetization	emu and emu/g
H	Magnetic field	tesla
H_{Hys}	Magnetic hysteresis	tesla
S	Entropy	$\frac{J}{K * Kg}$
V	Volume	m^3
ΔT_{ad}	Adiabatic temperature change during appliance of ΔH	K
ΔT_{fwhm}	Full-with-half maximum temperature span of a transition peak	K
RCP	Relative cooling power	$\frac{J}{Kg}$
q	Heat flow	$\frac{W}{g}$
E	Radiation energy	eV
C_p	Heat capacity	$\frac{J}{K}$

Abbreviations

RT	Room temperature
FOPT	First order phase transition
SOPT	Second order phase transition
MCE	Magnetocaloric effect
MCM	Magnetocaloric material
MST	Magnetostructural transition
MEA	Magetic equiatomic alloy
PM	Paramagnetic
FM	Ferromagnetic
AFM	Antiferromagnetic
DSC	Differential scanning calorimetry
XRD	X-ray diffraction
SEM	Scanning electron microscopy
PND	Powder neutron diffraction

Table of contents

Chapter 1

Introduction

1.1 Motivation

As the vapor-compression refrigeration technology was introduced to common households in the start of the 20th century [3], the technology quickly became indispensable. Today, 99 percent of all households in the United States have at least one refrigerator. About 26 percent has a second refrigerator and the number is expected to increase [4]. Also air-conditioning, which employs the same basic operating principle is now installed in three-quarters of all U.S households [5]. Although the average refrigerator efficiency has increased by 400 percent since 1974 [6], the increasing demand of cooling technologies implies the technology accounts for a significant part of residential energy consumption. This is confirmed by statistics from the Unites States, which is comparable the energy consumption of the rest of the western world. Today, cooling technologies account for 18.1 percent of total energy consumed in an average U.S. residential household. Figure 1.1 shows the U.S residential energy consumption in 2015 [7].

During the last decades, our society has become more energy conscious. In order to reduce emission of harmful greenhouse gasses and achieve a sustainable development of the future, the use of renewable energy sources is equally important as the introduction of innovative technologies that lead to a reduced energy consumption.

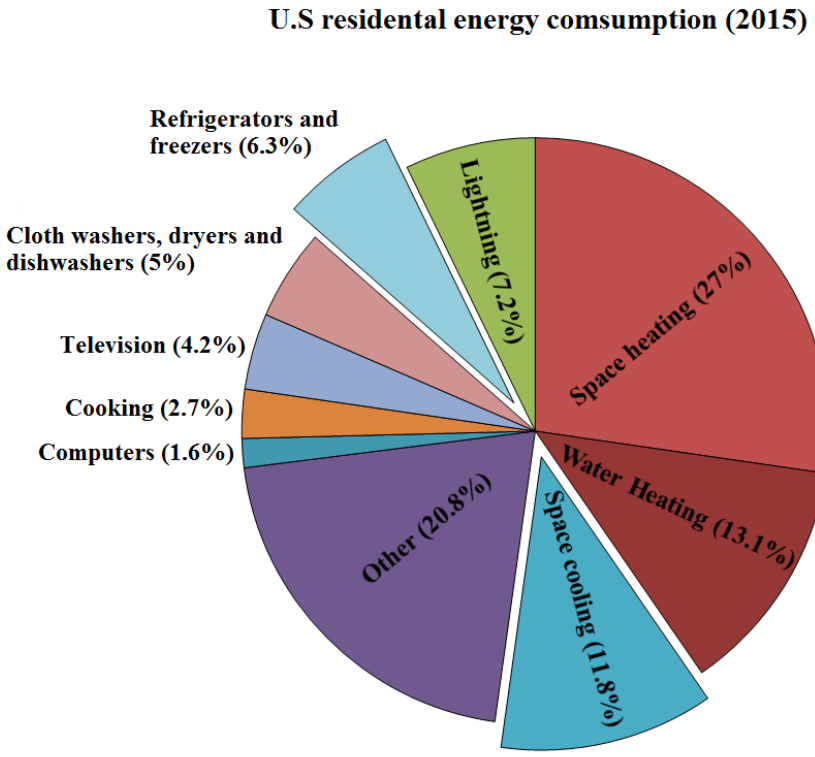

Figure 1.1: *The U.S residential end-use energy consumption of 2015. Cooling applications accounts for* 18.1 percent *of the total consumption. The figure is recreated from [5].*

The best commercial vapor compression technology is preforming at about 40% of its theoretical Carnot efficiency. During the past ten years there has been a growing interest in magnetic refrigeration as a new solid-sate cooling technology. Studies of magnetic cooling applications have predicted a Carnot efficiency of more than 60% [8].

The magnetic refrigeration technology utilizes a physical phenomenon called the magnetocaloric effect (MCE). The MCE is manifested by temperature change in a substance under application of a magnetic field variation [8]. Along with the potential of achieving a 20 to 30% higher efficiency [1], magnetic cooling technologies eliminate the need of hazardous refrigerant fluids and noisy compressors [8]. Due to recent technology advancements within the field, it has been suggested that the magnetocaloric effect will play an important role in future energy efficient and environmentally friendly cooling technologies [2]. A prototype of a magnetic heat pump used for wine cooling was demonstrated in 2015 [9]. Several factors are important in order to make magnetic heat pumps competitive in the refrigerator industry. Practical design for performance optimization is one obvious factor. But first priority is finding well suited magnetocaloric materials. The current research situation of this cooling technology revolves around finding good candidate magnetic refrigerants.

The number of papers published on magnetocaloric materials has increased significantly during the last years. There have been several candidate materials reported which show potential as magnetic refrigerants. Some of the MCMs currently considered for magnetic refrigeration near room temperature (RT) are mono and polycrystalline gadolinium, the $\mathrm{La(Fe,Si)_{13}}$ compound and the $\mathrm{MnFeP_{0.45}As_{0.55}}$ compound [8]. Additional materials and details are listed in table 2.2.

Another group of promising magnetocaloric materials is that of the magnetic equiatomic alloys (MEA). These compounds have a general formula MM'X, where M and M' are transition metals and X represents silicon, tin or germanium [2]. The alloys show interesting structural and magnetic behaviors for MCE applications. A giant MCE is reported as such an alloy undergoes a coupled magnetic and structural phase transition, a so called magnetostructural phase transition (MST). One possible MEA candidate is the MnNiGe compound. This alloy has a reported diffusionless, martensitic phase transition-temperature at 470 K upon heating, from a martensitic low temperature phase to a high temperature austenite parent phase. It has also been reported a paramagnetic-antiferromagnetic phase transition occurring at 346 K upon cooling [2]. Fe-substitution in the Mn or Ni site of the MnNiGe compound has been reported to reduce the martensitic transition-temperature and establish a MST [10]. Recent studies also indicate that Fe-substitution induces ferromagnetism in an otherwise antiferromagnetic alloy, which could lead to a giant MCE as the material undergoes a MST [2].

1.2 Research definition

The aim of this master thesis is to synthesize a series of Fe-substituted alloys: $Mn_{1-x}Fe_xNiGe$ (with $x = 0.03, 0.05, 0.07, 0.10, 0.15, 0.25$) and $MnNi_{1-x}Fe_xGe$ (with $x = 0.05, 0.10, 0.15, 0.25$) and investigate the samples' structural and magnetic properties. The structural and magnetic transition-temperatures as a function of Fe-substitution will be examined, and the influence of post-processing (heat treatment) the samples will be investigated. The primary objective of the thesis is to establish a magnetostructural coupling, investigate the potential for tuning the magnetostructural transition-temperature towards room temperature and further investigate the potential of the alloy as a magnetic refrigerant.

Chapter 2

Theoretical Background

2.1 The atomic structure of crystalline solids

2.1.1 The unit cell

To understand the material properties of a crystalline solid, it is necessary to map the structure of the substance at an atomic level. Crystallography describes the physical structure of crystallites mathematically as a three dimensional periodic arrangement of atoms, ions or molecules. A volumetric cell containing atoms with symmetry that uniquely defines the atomic structure of a crystalline solid is called a unit cell. Such a cell may be described by six lattice parameters. Figure 2.1 illustrates an example of a unit cell [11].

2.1.2 The space lattice and lattice points

A translation of the lattice parameters defines a three dimensional space lattice. The space lattice is build up by unit cells repeated in all directions to fill space until it produces a macroscopic crystallite [12]. The lattice points are shown as grey dots in figure 2.1. They are representing the center of gravity of atoms, ions or molecules in the cell. Each point is also a part of eight other cells in the surrounding space lattice. This means the unit cell in figure 2.1 constitutes a total of just one lattice point. Such a cell is called primitive. There also exist unit cells with more than one lattice point per cell, like the body-centered and face-centered unit cell [11].

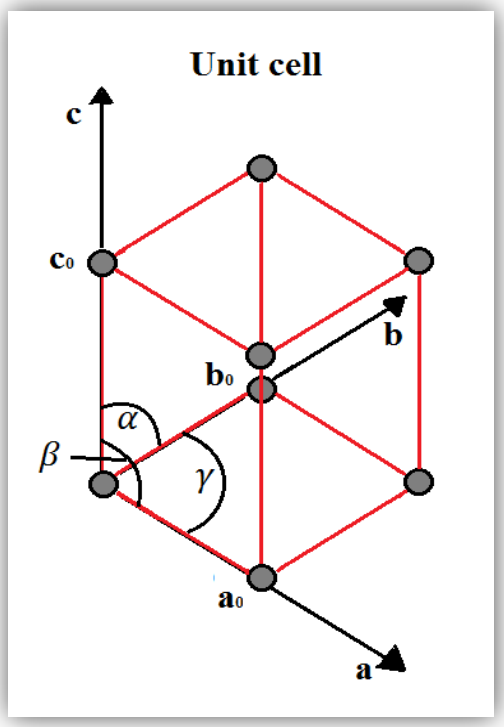

Figure 2.1: *A primitive tetragonal unit cell. The cell is in a crystallographic axis system spanned by a, b and c. Grey dots illustrate the lattice points and a_0, b_0 and c_0 are the lattice parameters for distance between lattice points and the origin of the crystallographic axis system. Lattice parameters α, β and γ describes the angles between the crystallographic axes.*

2.1.3 The crystal systems and Bravais lattices

There are a total of seven different crystallographic axial systems, called crystal systems. These are listed in table 2.1. Some of the crystal systems may be introduced to more lattice points without destroying symmetry of the cell. For example, a tetragonal unit cell may exist both as primitive and body-centered. The result is a total of 14 space lattices that represents 14 ways to fill space by a three dimensional array of points [11]. They are called the Bravais lattices. A crystalline solid has only one Bravais lattice, but there are still infinite number of ways to arrange atoms inside the three dimensional lattice. Figure 2.2 illustrates two of the Bravais lattice structures, the primitive hexagonal and primitive orthorhombic unit cell.

Table 2.1: *The seven crystal systems with their according lattice parameters [11].*

#	Crystal system	Lattice distance parameters	Angles ($^\circ$)
1	Cubic	$a = b = c$	$\alpha = \beta = \gamma = 90$
2	Tetragonal	$a = b \neq c$	$\alpha = \beta = \gamma = 90$
3	Hexagonal	$a = b \neq c$	$\alpha = \beta = 90, \gamma = 120$
4	Trigonal	$a = b \neq c$	$\alpha = \beta = 90, \gamma = 120$
5	Orthorhombic	$a \neq b \neq c$	$\alpha = \beta = \gamma = 90$
6	Monoclinic	$a \neq b \neq c$	$\alpha = \gamma = 90, \beta > 90$
7	Triclinic	$a \neq b \neq c$	$\alpha \neq \beta \neq \gamma \neq 90$

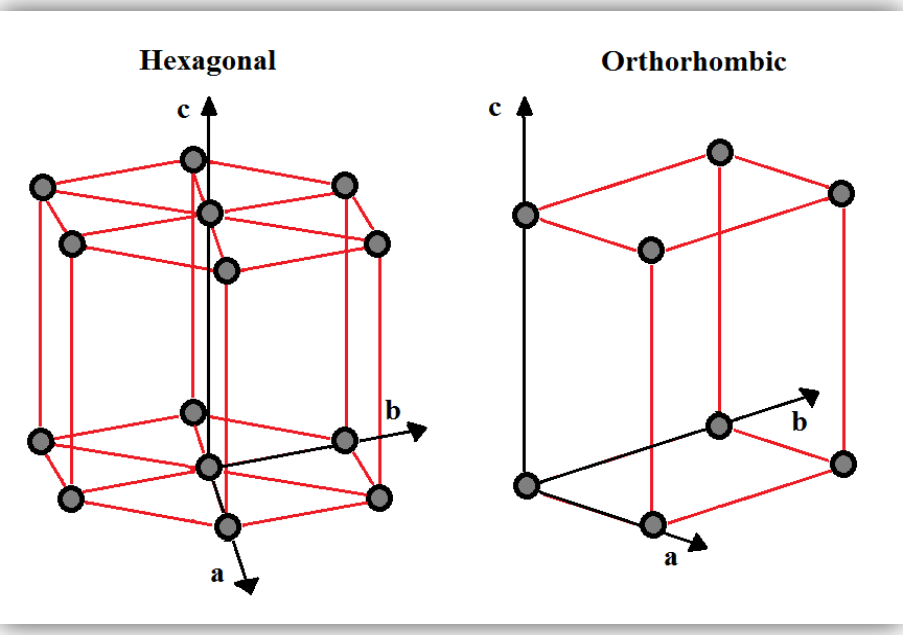

Figure 2.2: *The orthorhombic and hexagonal P-lattice unit cell with its crystallographic axes a, b and c. For the hexagonal unit cell,* $\alpha = \beta = 90, \gamma = 120$ *and* $a = b \neq c$*. For the orthorhombic unit cell,* $\alpha = \beta = \gamma = 90$ *and* $a \neq b \neq c$*. This illustration is inspired by [11].*

2.1.4 Miller indices

As the space lattice of a crystalline solid is symmetric and translational, sets of lattice planes (or atomic planes) will be repeated all the way through the crystalline solid. These atomic planes are described by Miller indices. The Miller indices are a three digit number (*hkl*) which describes an atomic plane according to its orientation and location in the unit cell [11]. The *h*, *k* and *l* values are given according to where atomic planes intersect the crystallographic axes a, b and c. For example the top plane of the primitive tetragonal unit cell in figure 2.1 has Miller indices (001), as it intersects the c axis at c_o [11].

2.1.5 Point groups and space groups

As manifested by the definition, it is the underlying symmetry of atoms, molecules or ions that determines the shape and size of a unit cell. There are several forms of symmetry used to uniquely define crystalline structures. The cell's rotation axes, inversion axes and mirror planes are three forms of symmetry often used to distinguish the atomic structure of a crystalline solid [11]. A combination of these point symmetry operations makes up a total of 32 unique point groups. The symbols $-1, -2, -3, -4, -6$ are used to denote the inversion axes, $1, 2, 3, 4, 6$ the *n*-fold rotation axes and *m* denotes mirror planes. These symbols are a part of the Hermann-Mauguin nomenclature indicating the different operations of symmetry [11].There also exist more complex symmetry operations like glide different planes (*a*, *b*, *c*, *n*, *d*, *e*) and screw axes ($\vec{s}$). A combination of the 32 point groups with the 14 Bravais lattices gives rise to 230 different space groups. A space group provides a complete description of the material symmetry [11].

2.2 Crystalline structure determination

2.2.1 Atomic planes

As explained in chapter 2.1.1, crystalline solids may be described as atoms stacked neatly in a periodic three dimensional lattice. This periodic arrangement means that sets of parallel atom planes are repeated periodically through the crystalline solid. An example of such an atomic plane is illustrated in figure 2.3. There may be several sets of atomic planes (called plane families) intersecting the unit cell in different ways. This depends on the crystalline structure. The distance d_{hkl} between the atomic plane families are of interest as they are distinctive for different materials [13].

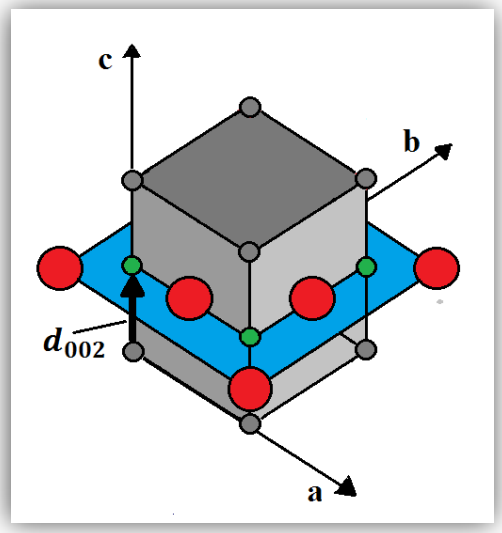

Figure 2.3: *Illustration of an atomic plane intersecting a unit cell. The atomic plane has miller indices (002) and is shown in blue. This atom plane consists of NaCl molecules. The red and green dots are illustrating the Na and Cl atoms. The vector $\vec{d}_{002}$ is pointing from the origin of the crystallographic axis system and intersects the (002) plane perpendicularly. The figure is inspired by [13].*

2.2.2 X-ray diffraction

X-ray diffraction is a method for determining the interatomic distance d_{hkl} between these sets of atomic planes called plane families. As illustrated by figure 2.4, this is done by radiating photons towards the crystalline solid with an incident angle θ. As radiation hits the crystalline solid, some of the photons are scattered off the first plane and some are transmitted to the next. As photons transmit trough the planes, some light is scattered off each plane, leading to sets of scattered waves leaving the crystalline solid. Since the atomic planes are parallel to each other, the scattered waves will have the same exiting angle (θ_2) as the angle of incident radiation (θ_1). As θ_1 is varied, the distance photons have to travel through the medium changes. Thereby, parallel scattered waves leaves the medium with a phase shift $\varphi(\theta_1)$. This leads to constructive interference at some values of θ_1 [13]. The constructive interference is observed as diffraction peaks by a detector observing the scattered waves.

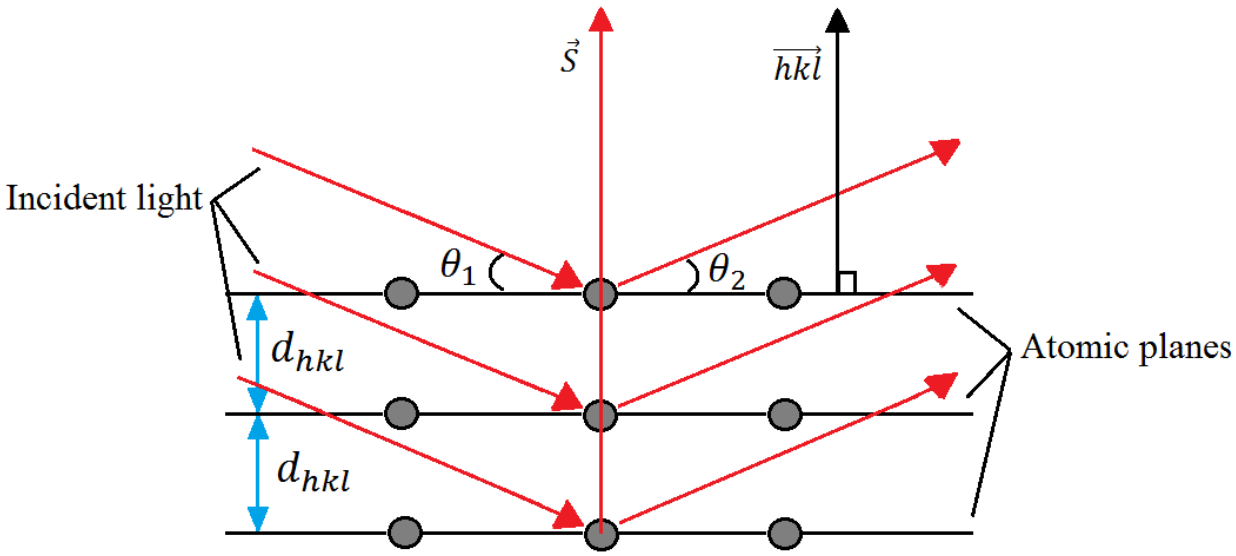

Figure 2.4: *A schematic drawing of incident radiation hitting the lattice planes of a crystalline solid. The vector $\vec{S}$ bisects the angle between the incident and scattered radiation. The $\overrightarrow{hkl}$ vector is perpendicular to the lattice planes, d_{hkl} is the interatomic distance between the planes, and the grey dots illustrate the basis-elements in the lattice. The incident and scattered radiation is denoted as θ_1 and θ_2. The figure is inspired by [13].*

2.2.3 Bragg's law

Equation 2.1 describes Bragg's law, which is the criterion for constructive interference of the scattered waves [13].

$$n\lambda = 2d_{hkl}\sin(\theta) \qquad n \in \mathbb{Z} \quad \textbf{(2.1)}$$

This means that when a diffraction peak is observed, the interatomic planar distance d_{hkl} for this plane family may be calculated. This is possible since the wavelength (λ) of incident radiation is constant and known, and the incident radiation angle θ for that exact peak may also be measured in such an experiment. It is noteworthy that the radiation wavelength has to be in the same regime as the interatomic distance between the atom planes. This distance is usually a few angstroms, which is the reason why X-rays are used [12].

Another criterion for constructive interference is that the $\overrightarrow{hkl}$ and $\vec{S}$ vector are parallel to each other. This only occurs at certain crystallite orientations [13]. Since a powdered sample contains thousands of crystallites oriented randomly, there is a good chance incident radiation will hit some crystallites with the right angle [13]. Intensity of the diffraction peaks depends on the arrangement of atoms in the plane, and the number of electrons in the atom. The more electrons, the more intensely X-rays are scattered.

As scattered X-rays have been detected in a given 2θ angular interval, the scattered photon intensity may be plotted as a function of the angular interval. This maps all the diffraction peaks as a diffraction pattern. Each peak describes one plane family in the crystallite solid. These planes are indicated by miller indices. By accurately determining all the peak positions and running the graph through a database, the phase of the material may be identified by comparing scans of known samples [13].

2.2.4 Radiation disturbance

As electromagnetic radiation hits a material, other interactions may also occur depending on the energy, intensity and wavelength of the incident radiation. John Willey explains in his book ¨Nuclear physics -Principles and Application¨ three different ways photons may interact with matter; by the photoelectric effect, Compton scattering and pair production [14].

Compton scattering is happening when an incident photon hits a free electron. The photon will scatter depending on the angle of impact. It also loses some energy, as this is transmitted to the recoiling electron.

In the case of pair production, the photon energy is completely converted into the creation of an electron-positron pair. This effect does not have a relevant cross section until the incident photon energy E_γ reaches several MeV.

The photoelectric effect occurs when an incident photon fully transmits its energy (E_γ) to an atomic bound electron and ionizes the atom. Another electron from a higher shell will then fill this space. This results in emission of a photon and an ejected electron.

In the case of X-ray photons probing crystalline solids, the energy levels are too low for the pair production and Compton scattering effect to take place [14]. The emitted photons from the photoelectric effect can contribute to the background noise of the diffraction pattern. Incident photons may also excite electrons by knocking them to a higher shell. As this electron is de-excited, a photon is emitted. This is called a fluorescence effect, which will decrease diffracted radiation hitting the detector and increase background noise. Some elements like Co, Fe and Mn expel more fluorescence as they absorb more of the incident radiation. To compensate for this, some detectors in a XRD-device are designed to remove the fluorescent radiation [13].

2.2.5 Neutron diffraction

The established diffraction theory explained in chapter 2.2.1 to 2.2.3 may also be applied to neutron diffraction. Neutrons will scatter off atoms and create distinctive diffraction patterns. As neutrons have no charge, they will not interact with atomic bound electrons, but rather the atomic nuclei [19]. Unlike X-ray scattering, for neutron scattering there exists no systematic correlation between the scattering power of an element and its atomic numbers (position in the periodic table). This makes it possible to distinguishing elements with approximately the same atomic number. This is impossible with X-ray diffraction since the different electron density of neighboring elements (their scattering power) is too small to be resolved [C. Frommen, personal reference].

Since neutron-matter interactions are relative weak and neutrons can penetrate several millimeter of steel/aluminum, it is possible to use complicated sample chambers withstanding extreme temperature and pressure values [18].

2.3 Magnetism

2.3.1 Magnetic moment

Every atom has a magnetic dipole moment. This is due to the electrons orbital movement around its nucleus and also the electrons intrinsic spin around its center of gravity [15]. Consider the Bohr atomic model of a hydrogen atom. This situation is illustrated in figure 2.5. The orbiting electron creates a current loop circuit around its nucleus. The product of this current and the area of the loop defines the magnetic moment, $\vec{\mu}$ of the atom. This vector has the SI unit ampere-square meter (Am^2) and a given direction [15]. The magnetic moment intersects the plane spanned by the orbiting electron perpendicularly and its direction is determined by the right hand rule.

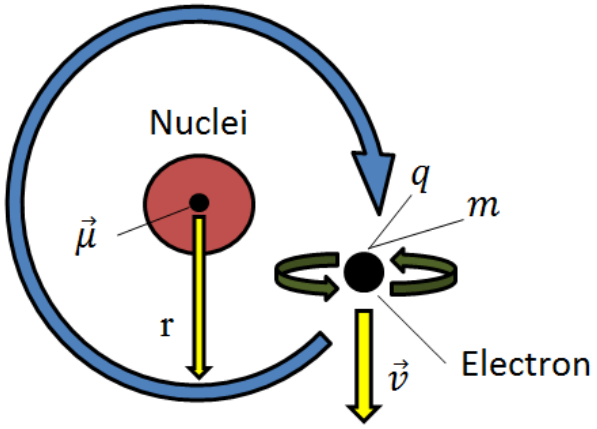

Figure 2.5: *An illustration of the hydrogen atom. The electron (black) with mass* m *and charge* q *is orbiting its nucleus (red) with the speed and direction* $\vec{v}$*. The electrons looping path is indicated by the blue arrow and the intrinsic electron spin around its own center of gravity by the two green arrows. The distance between the nuclei center and the current loop circuit is denoted by radius r. The plane spanned by the orbiting electron is intersected perpendicularly by the magnetic moment μ pointing out of the paper indicated by the black arrow tip.*

2.3.2 The magnitude of magnetic moments

As mentioned, both the electron orbital movement around its nucleus and spin around its center of gravity contribute to the magnetic moments. The calculation of the electrons magnetic moment due to its orbital movement (μ_L) may be done semiclassically. Consider the angular momentum (L) of an electron orbiting its nucleus. This is given by classical physics as:

$$L = mvr \qquad \textbf{(2.2)}$$

In equation 2.2 m is the electron mass, v is the speed of the electron and r is the radius of the electrons current loop circuit to the center of the loop [15]. The orbital magnetic moment is defined as:

$$\mu_L = IA = I\pi r^2 \qquad \textbf{(2.3)}$$

Here, I is the current in the loop circuit and A is the area covered by the loop. The loop current may be written as a charge passing a point per unit of time, in other words the particle charge (q) divided by the time an electron uses to complete one loop (T). The period T is further given the distance traveled ($2\pi r$) divided by particle velocity (v). This gives:

$$I = \frac{q}{T} = \frac{qv}{2\pi r} \qquad \textbf{(2.4)}$$

Combining equation 2.3 and 2.4 gives:

$$\mu_L = \frac{qv}{2\pi r}\pi r^2 \qquad \textbf{(2.5)}$$

By introducing equation 2.2, we get

$$\mu_L = \frac{q}{2m}L \qquad \textbf{(2.6)}$$

The quantum of angular momentum is h-bar ($\hbar$). By introducing direction of the angular momentum, h-bar and the electron charge ($-e$) to equation 2.6, we get:

$$\overrightarrow{\mu_L} = \frac{-e\hbar}{2m}\frac{\vec{L}}{\hbar} \qquad \textbf{(2.7)}$$

By using equation 2.7, the magnetic moment for a charged particle (q) with mass m and angular momentum L around the nucleus may be calculated. As mentioned, intrinsic spin also contributes to the magnetic moment. Paul Dirac predicted in 1927 by the use of quantum mechanics and the relativistic Dirac wave equation that the magnetic moment due to electron spin ($\overrightarrow{\mu_s}$) is twice the value given by its orbital movement. This is confirmed by experimental data, which indicates a multiplication factor value of 2.00232, the so called *g-factor* [15].

$$\overrightarrow{\mu_S} = -2 * \frac{e\hbar}{2m}\frac{\vec{S}}{\hbar} \qquad \textbf{(2.8)}$$

A quantum unit μ_B may be introduced as:

$$\mu_B = \frac{e\hbar}{2m} \qquad \textbf{(2.9)}$$

μ_B is called the Bohr magneton and is a quantum factor of magnetic moments. It has a value of $9.27 * 10^{-27}\text{Am}^2$. Calculating the total magnetic moment of all the electrons in an atom becomes complicated. By summarizing the coupling of electron spins and orbital movements, theoretical calculations estimate atoms having magnetic moment values of a few Bohr magnetons. This fits well with experimental data [15]. The magnetic field from one atom having a magnetic moment of one Bohr magneton may be calculated as:

$$\mu = \mu_B\mu_0 \qquad \textbf{(2.10)}$$

This gives a magnetic field of $1.16 * 10^{-29}$ T per atom. In equation 2.10, the factor $\mu_0 = 4\pi 10^{-7}\,\frac{\text{Tm}}{\text{A}}$ is the magnetic permeability constant of free space [15].

2.3.3 Magnetization of materials

The magnetic moment of each atom is clearly very weak, and as they are randomly oriented inside a material, they will cancel each other out. The randomness of magnetic moments is caused by thermal vibrations, which tend to disorientate the moment directions. Also, little interaction between neighboring atoms causes this randomness to persist. This is why most materials are not magnetic. A different situation occurs when magnetic moments are aligned in the same direction. In this case, a net magnetic field is produced from all the aligned and coupled magnetic moments. One way to achieve alignment of magnetic moments is to reduce the temperature of the material, which reduces the thermal vibrations. Another possibility is to introduce an external field. This aligns the magnetic moments in parallel with the field. The process is called magnetizing the material, which could intensify an external magnetic field by a factor of several thousand depending on the material [15]. The magnetization of a material ($\vec{M}$) is defined by the following equation:

$$\vec{M} = \frac{\delta\vec{\mu}}{\delta V} \qquad \textbf{(2.11)}$$

In equation 2.11, $\vec{\mu}$ is the net magnetic dipole moment and V is the volume of the material. The total field may further be calculated as:

$$\vec{H}_{\text{tot}} = \vec{H}_{\text{app}} + \mu_0 \vec{M} \quad \textbf{(2.12)}$$

Where $\overrightarrow{H_{\text{tot}}}$ is the total magnetic field, $\overrightarrow{H_{\text{app}}}$ is the applied external field and μ_0 the permeability constant. Rewriting equation [2.12] gives:

$$\vec{H}_{\text{tot}} = H(1 + X_m) \quad \textbf{(2.12)}$$

Where $X_m$is called the magnetic susceptibility. By substituting X_m by the relative permeability factor ($K_m = 1 + X_m$), equation 2.12 may be written as:

$$\vec{H}_{\text{tot}} = K_m \vec{H}_{\text{app}} \quad \textbf{(2.13)}$$

Several quantum models are derived for determining the magnetization of crystalline matter. The Heisenberg model calculates interaction energies by summarizing spins located in the space lattice and a coupling constant of neighboring spins. This model is explained in details by P. Papon, J, Leblond and P.H.E Meijer in the book Nuclear Physics –Principles and Applications [20]. The magnetization of a magnetic material may also be determined experimentally with a magnetometer such as the physical property measurement system (PPMS) from Quantum Design used throughout this master thesis.

2.3.4 Magnetic permeability and susceptibility

The relative permeability (K_m) and the magnetic susceptibility (X_m) describes the materials ability to create a magnetic field within itself upon magnetization from an external field. Materials are generally classified into three categories depending on how their magnetic moments behave in an external magnetic field; paramagnetic, ferromagnetic and diamagnetic materials. The magnetic susceptibility (X_m) for paramagnetic and diamagnetic materials is in the order of 10^{-5} , while for ferromagnetic materials it can be a factor of several thousand.

2.3.5 Types of magnetic materials

Paramagnetic materials: The magnetic dipoles in these materials hardly interact with each other and are usually randomly orientated. By application of an external field at room temperature (RT), the magnetic dipole moments are partly aligned, but not with any significant effect. This is because the materials have values of thermal energy more than 200 times greater than the energy associated with magnetic moments alignments [15]. Thermal motion tends to disorientate any alignments of magnetic moments and reduces the magnetization effect [15].

Ferromagnetic materials: In ferromagnetic materials such as cobalt, iron or nickel, the electrons (inducing the magnetic dipole moments) interact strongly with each other. Because the magnetic dipole moments exert strong forces on their neighbors, these materials have a large magnitude of susceptibility (X_m). Under appliance of a small external magnetic field, a large degree of alignment can occur. The areas where magnetic moments are aligned are called magnetic domains. These areas tend to expand or change direction towards the direction of the external field. The total induced field in a ferromagnetic material can be a factor of 500 to 100 0000 greater than the applied field [15], as the magnetic susceptibility is large (see equation 2.13).

Ferromagnetic material may also form two groups of spins in the sub lattice, which are aligned in antiparallel directions. This is called *antiferromagnetism* and results in a reduction of the total magnetization. In addition a *ferrimagnetic* and *helimagnetic* state exists. In a ferrimagnetic state, antiparallel moments are of different magnitudes which also results in reduction in the total magnetization. The helimagnetic state is characterized by magnetic moments aligned in helices [16].

Diamagnetic materials: Diamagnetic materials have their magnetic dipole moments orientated in the opposite direction of the external field. Just as for ferromagnetic materials, the induced magnetization is much larger than the external magnetic field. This results in a total net magnetic field orientated in the opposite direction of the applied field [15].

2.3.6 Magnetic hysteresis

When the external magnetic field is removed, a ferromagnetic material will not demagnetize in the same way it became magnetized. This is caused by the shift of magnetic domains, which is not entirely reversible. The magnetic domains tend to remain in some degree the way they got aligned by the external magnetic field. When magnetization remains after the field is completely removed, the material has become a permanent magnet. This effect is called magnetic hysteresis. The hysteresis curve showed in figure 2.6 illustrates a plot of the applied magnetic field (H_{app}) versus the magnetic field (*H)* due to material magnetization. The gray shaded area within the complete cycle is proportional to the energy converted to heat during one cycle [15].

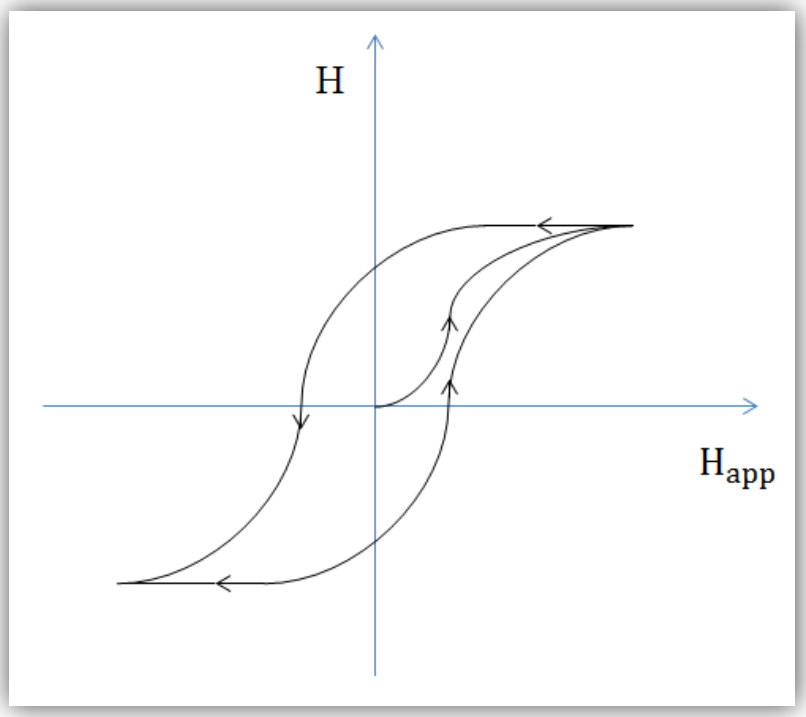

Figure 2.6: *A ferromagnetic material being magnetized (from the origin of the axis system) by an external applied field (H_{app}). As this field is removed, the material remains magnetized due to the remaining alignment of the magnetic moments. By applying a reversed field, the magnetic dipoles will now also align in the other direction. By reversing the external field once more, the magnetized material ends up with the same alignment of magnetic moment as the first time. The area within the complete cycle gives the amount of energy converted to heat during one magnetizing cycle. The graph is inspired by [15].*

2.4 Thermodynamics of phase transitions

2.4.1 Thermodynamic potential

Different matters have a wide range of properties. Even a homogenous substance with a fixed chemical composition may exist in several states and phases expressing various properties. As the intensive variables of a system changes (like temperature, pressure, magnetic field or electric field) its phase may become unstable. In that case, a phase transition occurs. This is manifested by a change in the substance's properties [16]. An example is the variation in structural, optical, and mechanical properties of H_2O, as an intensive variable like temperature and pressure are increased or decreased.

The properties of a substance, which determines its phase, may be described at an atomic level by intermolecular potentials or interactions between particles. This makes the field of thermodynamics applicable for description of phase transitions [16]. Thermodynamic potentials obtained by Legendre transformations can be used to describe the thermodynamic state of a system.

$$\Delta G(p, T_{const}) = \Delta H - T\Delta S \qquad \textbf{(2.15)}$$

The Gibbs free energy *(G)* is such a thermodynamic potential. Equation 2.15 describes the available energy that can be used to do work. The energy is given as the product of temperature T and change in entropy ΔS subtracted from the change in enthalpy ΔH of the system during a reaction. T_{const} and p is the constant temperature and pressure value of the system. In order to have a stable phase, the thermodynamic potential should be low. In processes involving chemical reactions, favorable or spontaneous reactions occur as $\Delta G < 0$ [16]. In systems with variables other than temperature and pressure, different thermodynamic potentials may be used to describe the system.

2.4.2 First and second order transitions

Ehrenfest classified in 1933 two types of phase transitions; first and second order transitions. A first order phase transition (FOPT) has discontinuities in its first order derivatives of the Gibbs free energy, with respect to the state variables T and p. Both the entropy (equation 2.16), and volume (equation 2.17) are discontinuous during a FOPT (see figure 2.7) [16]. Another distinctive property of a FOPT is the involved latent heat.

An example of a FOPT is liquid H_2O vaporizing to a H_2O gas. Latent heat is needed in order break the molecular bonds and results in volume and entropy values making a huge leap as the temperature of the substance passes 100 ℃ at one atm.

$$(\frac{\delta G}{\delta T})_P = -S \qquad \textbf{(2.16)}$$

$$(\frac{\delta G}{\delta p})_T = V \qquad \textbf{(2.17)}$$

A second order phase transition (SOPT) on the other hand, has continuous first order derivatives of Gibbs free energy, but some of the second derivatives are reduced to zero or diverge. SOPT has no latent heat involved and are usually related to electron properties [16].

2.4.3 Magnetic phase transitions

As explained in chapter 2.3.5, a crystalline solid can exist in several magnetic states. The magnetic state of a substance is related to the substance's magnetic spin orientations. Magnetic spins are located on lattice points in the crystalline space lattice and they are orientated in different ways depending on a substance's intensive variables and material properties. The spins are influenced by lattice vibrations, particle interactions, and the magnitude of any external magnetic field [16]. This means that a magnetic phase transitions may be triggered by temperature regulations, by introducing an external magnetic field or by introducing new elements to a substance modifying its atomic structure and composition. Magnetic phase transitions may occur both as first and second ordered. The temperature point where a paramagnetic-ferromagnetic (PM-FM) transition occurs is called the Curie temperature (T_C) and the temperature point where a paramagnetic-antiferromagnetic (PM-AFM) transition occurs called the Neel temperature (T_N) [16].

Figure 2.7 compares two magnetic materials introduced to a magnetic field change ΔH [6], one material with FOPT characteristics and one with SOPT characteristics. The phase transition in both cases is a PM-FM transition occurring at the temperature point ($T_{c)}$.

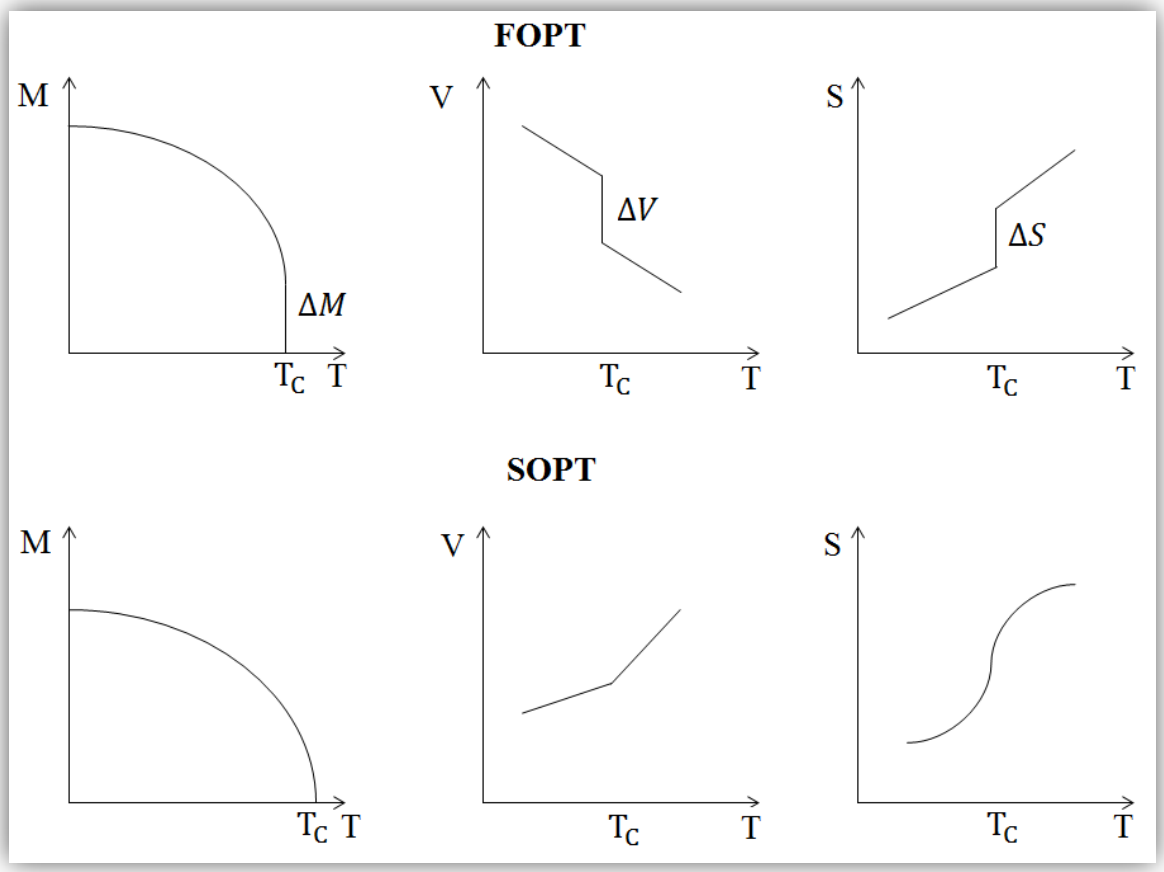

Figure 2.7: *Comparative plots of first and second order phase transitions according to change in magnetization (M), volume (V) and entropy (S). The first and second order magnetic transitions are triggered by the introduction of an external magnetic field (ΔH). The transition occurs at the transition-temperature (T_c). The figure is recreated from [6].*

2.4.4 Structural phase transitions

Since different phases involve such a high variety of properties, it is difficult to give a satisfactory typology of all transition types. Thermodynamics lay the foundation for classification by differentiating first and second order phase transitions. Another grouping of transitions is the ones involving a structural transformation [16].

Structural phase transitions describe the process of materials undergoing a change in atomic structure. Some structural transitions are not associated with macroscopic diffusion, but rather solid-solid transformations. A solid-solid transformation involves a crystalline solid undergoing a microscopic change in its atomic space lattice. This occurs as atomic displacements or molecular rotations forces atoms to move from their equilibrium to a new position. The result is a new lattice with different symmetries. A translation like this does not happen instantaneously at the transition-temperature point (T_s). Due to restoring forces as atoms are moved from their equilibrium positions, the transition is initiated at temperatures higher or lower than (T_s) [16]. This is associated with thermal hysteresis. A sufficient reduction of temperature will trigger a structural phase transition and form space lattice structures of lower symmetry than the initial space lattice. In the same way, sufficiently increasing the temperature of a crystalline matter will create structural phases with higher symmetry [16]. The structural transitions (T_s) temperatures of different crystalline solids vary a lot, but may be tuned by doping the material with different elements.

One type of structural transition is the martensitic transformation. This is a diffusionless transformation caused by atomic motions in the crystalline space lattice [16]. When lattice distortion becomes large, the phase becomes unstable and the solid undergoes a structural phase transition. This transition is associated with a change in lattice parameters and thereby a volume-change of the unit cell. The transformation is of first order and it modifies the mechanical properties for the crystalline material. It is initiated by nucleation-growth process. Nucleation occurs as germs are formed by diffusion and represent a new phase in the substance. The germs initiate a phase transition and grow rapidly ($10^5 \frac{\mathrm{cm}}{\mathrm{sec}}$) until the new phase is formed [16]. One common example of a martensitic transformation is the procedure of hardening steel. In this process, a high temperature Fe – C mixture (austenite) forms hardened steel (martensite) upon quenching.

2.5 The magnetocaloric effect

As discussed in chapter 2.3.3, introduction of an external magnetic field (*H*) to a crystalline solid may trigger an alignment of magnetic spins in the substance, in other words a PM-FM transition. With the right material and magnitude of the magnetic field, this magnetic transition can occur at RT. A PM-FM transition will cause a reduction in the magnetic entropy (S_{mag}) of a crystalline sold, as randomness is removed from the system. By application of the external field under adiabatic conditions, S_{mag} is reduced but the total entropy (S_{tot}) will not change. This reduction of S_{mag} is compensated by an increase in the phonon term (S_{ph}), which corresponds to lattice vibrations [6]. An increase in lattice vibration leads to a temperature rise in the crystalline matter (ΔT_{ad}). This physical phenomenon is called the magnetocaloric effect (MCE), which is manifested by temperature change in a substance under the appliance of a magnetic field variation. Step one to step two in figure 2.8 illustrates the MCE.

2.5.1 Magnetic heat pumps

Under adiabatic conditions, the MCE may be utilized to create a solid state heat pump [6]. Figure 2.8 illustrates four stages where mechanical work in form of magnetic field variations is converted into cooling power. As heat evolved from the MCE is removed, the total entropy of the system is thereby lowered. This is illustrated by stage two and three in figure 2.8. An adiabatic demagnetization of the substance at stage 3 results in a temperature reduction. This leaves the substance at stage four below the initial start temperature (RT). The cycle may be repeated as the substance is heated back to RT. A magnetic heat pump is created. Clearly, a device utilizing the magnetocaloric effect may be used both for heating and cooling applications, but the main interest is currently of the cooling applications. As mentioned in the introduction, studies of magnetic cooling applications have predicted a Carnot efficiency of more than 60% [6].

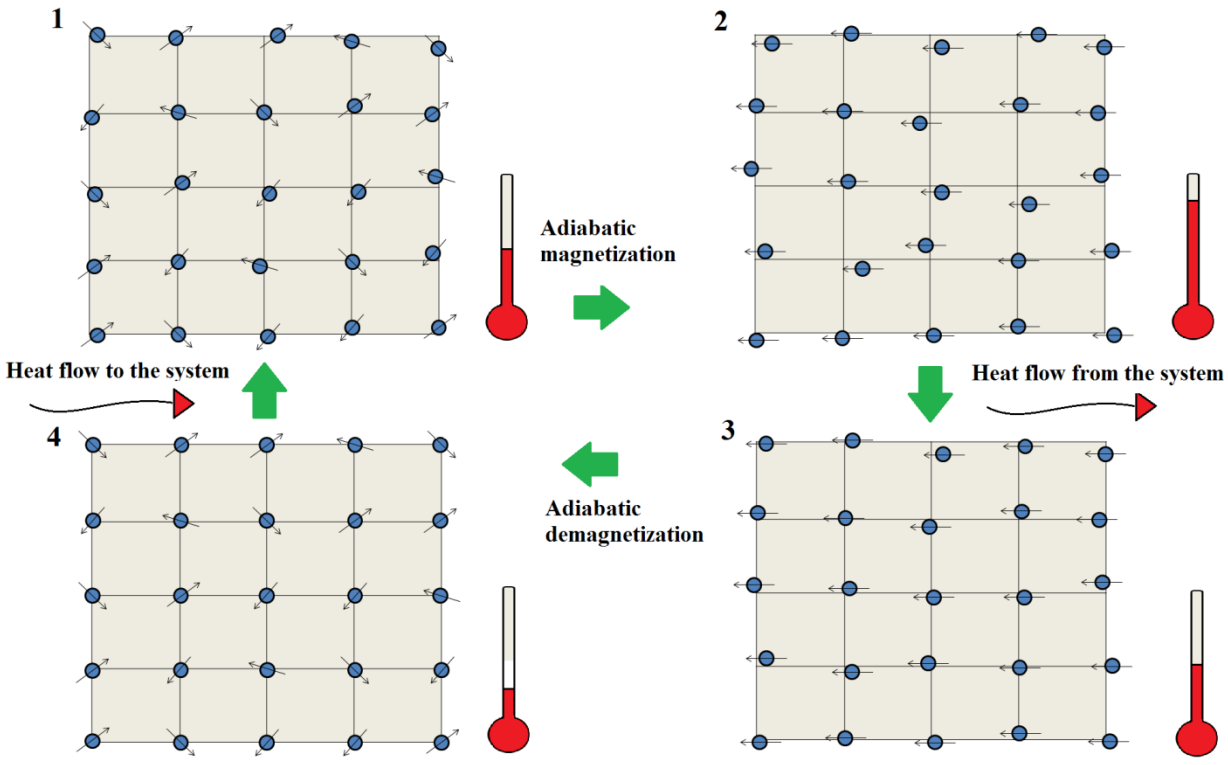

Figure 2.8: *A schematic drawing of a magnetic heat pump. Two dimensional crystalline lattices are illustrated as black matrices. Blue dots illustrate atoms with their corresponding spin directions represented by vectors. The atomic displacement from lattice vertices illustrates lattice vibrations. A paramagnetic material at room temperature (situation one) is magnetized adiabatically. As a result, the lattice vibrations increase (situation two). Heat transfer is then reducing the crystalline temperature back to initial room temperature (situation three). An adiabatic demagnetization reduces the temperature further. This refrigerated material may be used for cooling applications (situation four). The thermometers illustrate the relative temperature at the four different stages of the cycle. This illustration is inspired by [6].*

For its simplicity, a permanent magnet is desired as the external magnetic fields source. This limits the external field magnitude to approximately two tesla. However, a field of such a magnitude is sufficient for triggering a magnetic phase transition. Several factors are important in order to make magnetic heat pumps competitive in the refrigerator industry. Practical design of the magnetic heat pump for performance optimization is one obvious factor. But first priority is finding well suited magnetocaloric materials (MCM's). The current research situation of this cooling technology revolves around finding good candidate magnetic refrigerants.

2.5.2 Magnetocaloric materials

In the search of MCMs, many aspects have to be taken into consideration. An ideal MCM should have a large entropy change (ΔS) upon a magnetic phase transition coupled with low magnetic and thermal hysteresis (ΔH_{hys} and ΔT_{hys}). In addition, a large adiabatic temperature change (ΔT_{ad}) in a moderate magnetic field (less than two tesla) is desired. Other important aspects are the ability to withstand strain from a long cyclic lifetime, availability and environmental friendliness [6].

The magnetic transition type is important for prediction of material performance, as it has a strong influence on ΔS. MCMs are mainly classified into two groups; first order phase transition (FOPT) and second order phase transition (SOPT) materials [6]. As discussed in chapter 2.4.2, a FOPT is associated with discontinuity of magnetization, volume and entropy of the material. This results in an entropy change (ΔS) significantly larger than what occurs in SOPT's. The relatively large ΔS in FOPT is often referred to as transitions with a giant MCE. FOPT with a giant MCE may be related to spin-reorientation or a magnetostructural transition. A magnetostructural transition is manifested by a coupled magnetic and structural (recall chapter 2.4.3) phase transition which results in a large ΔS [6]. SOPT have smaller ΔS values, but are also associated with smaller amount of hysteresis. Hysteresis in a MCM is associated with effect loss in a magnetic heat pump device as an additional magnetic field (ΔH_{hys}) is needed to reorient the magnetic domains during a MCE cycle (recall chapter 2.3.6) and compensate for thermal losses. Non-magnetic properties like grain size and porosity of magnetic powders should also be taken into consideration as this influences ΔS.

2.5.3 Magnetocaloric effect measurements

A complete description of the MCE in MCM's is given by the entropy change $\Delta S(T, \Delta H)$ and the adiabatic temperature change $\Delta T_{ad}(T, \Delta H)$ [6], where ΔH is the external magnetic field variation and T is the magnetic refrigerant temperature. As mentioned in the introduction of this chapter, the magnetic entropy change ΔS_{mag} will directly influence the lattice entropy (S_{ph}). Thereby, the entropy change related to magnetization of the material describes the total entropy change (ΔS) during the transition [6]. The value may be calculated by integrating the Maxwell relation:

$$\Delta S(T, \Delta H) = \int_{H_i}^{H_f} \left(\frac{\partial M(T,H)}{\partial T}\right)_H dH \qquad \textbf{(2.18)}$$

In equation 2.18 H_i and H_f represent the initial and final magnetic field values, M is the magnetization and T is the temperature of the MCM. The magnetization derivate has its maximum value during a magnetic phase transition, which is the reason a magnetic transition is desired for large a MCE. The adiabatic temperature change may be calculated as:

$$\Delta T_{ad}(T, \Delta H) = -\int_{H_i}^{H_f} \left(\frac{T}{C_p(T,H)}\right)_H * \left(\frac{\partial M(T,H)}{\partial T}\right)_H \partial H \qquad \textbf{2.19}$$

From equation 2.19, it is clear that determination of ΔT_{ad} requires knowledge of the heat capacity C_p in addition to the magnetization of the material.

2.5.4 Direct and indirect measurements

There are different ways to determine ΔS and ΔT_{ad} values of a MCM. Direct measurements involve measuring ΔT_{ad} directly as a material is magnetized by an external field. This requires good thermal isolation and a fast magnetic field change in order to achieve adiabatic conditions [6]. The ΔS value may be directly measured with a differential scanning calorimetry with a magnetic field source which may trigger the phase transition. Although the measurement is straight forward, the lack of commercial equipment limits the possibilities of direct measurements.

Indirect measurements are a widely adopted technique. In this case, heat capacity values are acquired from DSC measurements (with a magnetic field source) and magnetization values from magnetic measurements. The MCE is further calculated from the acquired data [6].

2.5.5 Cooling power

In order to compare different MCM's performance as magnetic refrigerants, the relative cooling power term is introduced. A MCM's relative cooling power (RCP) is given as the product of the total entropy change (ΔS) and the full-with-half maximum temperature span (ΔT_{fwhm}) of the transition peak, given by ΔT_{ad} [17].

$$RCP_{\Delta S,(\Delta T_{ad}>2K)} = \Delta S \Delta T_{\mathrm{fwhm}} \qquad \textbf{(2.20)}$$

The limitation of $\Delta T_{ad} > 2K$ is set as the minimum adiabatic temperature span. Values below this limit become difficult to utilize in a magnetic heat pump device [6]. Relative cooling power indicates how much heat can be moved from a cold to hot environment by the MCM in a magnetic heat pump.

2.5.6 Current situation on magnetocaloric materials

There has been reported several candidate materials showing potential as magnetic refrigerants during the last decade. Some of the MCMs currently considered for magnetic heat pumps are listed in table 2.2 [6].

Table 2.2: *Different candidate materials for the MCE close to room temperature [6].*

MCM	$\boldsymbol{T_{peak}}$(K)	$\boldsymbol{H_f}$(T)	$\Delta \boldsymbol{S_{max}}(\frac{\mathrm{J}}{\mathrm{Kg} * \mathrm{K}})$	$\Delta \boldsymbol{T_{ad,max}}$ (K)
Single crystal Gd	295	2	6.2	5.2
$Gd_5Si_2Ge_2$	277	2	15	5
$LaFe_{10.92}Co_{0.98}Si_{1.1}$	293	1	5.3	1.2
$MnFeP_{0.45}As_{0.55}$	303	1	13	2.8
$La_{0.67}Ca_{0.33}MnO_3$	268	2	6.9	2.4

High purity gadolinium is a good magnetocaloric material and often serves as a benchmark for comparing the MCE in new materials. It is however very expensive, at about €2000 per 300g (approximate amount needed for a magnetic refrigerator) [21].

The $Gd_5Si_2Ge_2$ compound shows a simultaneous change of symmetry and magnetic order and exhibit a giant MCE [22]. This compound is dependent on proper heat treatment as rare earth elements often contain interstitial impurities like H, C, N and O. The main drawback for this compound is the high price, and relative high hysteresis losses [23].

The $La(Fe,Si)_{13}$ based materials crystalizes in a cubic structure and show an ordering temperature between 200 and 262 K with a sharp first order magnetic transition leading to a large MCE [24, 25]. An itinerant metamagnetic (IEM) transition is observed above this critical transition-temperature. By Co-substitution (for example $LaFe_{10.92}Co_{0.98}Si_{1.1}$), the critical transition-temperature can be tuned towards RT [26, 27, 28]. A major drawback for this compound is the change in lattice parameters which may cause long-term cycling problems as the polycrystalline material becomes granular [29].

2.5.7 Magnetic equiatomic alloys

As mentioned in the introduction, another group of MCMs with interesting characteristics for MCE applications are the magnetic equiatomic alloys (MEA). The MEA compounds have a general formula MM'X, where M and M' is transition metals, and X represent silicon, tin or germanium. The intermetallic alloy MnNiGe synthesized in this thesis is such an MEA [8].

The MnNiGe compound has a high temperature austenite parent phase with a hexagonal unit cell structure (see fig 2.2). This austenite exists in a paramagnetic state [10]. A martensitic (structural) phase transition is reported at 470 K, where an orthorhombic martensite phase is created upon cooling the austenite parent phase [8]. This low temperature martensite has an orthorhombic unit cell structure (see figure 2.2). The MnNiGe compound has distinctive magnetic properties as it undergoes a PM-AFM phase transition. The reported Neel temperature (T_N) is 346 K upon cooling from the PM to AFM state. The compound has a spiral atomic structure and as discussed in section 2.3.5, the AFM state has its magnetic spins oriented antiparallel [8].

2.5.8 The MnNiGe compound with Iron substitution

Induced ferromagnetism in the antiferromagnetic alloy MnNiGe has been achieved by Fe-substitution on the Mn or Ni site ($Mn_{1-x}Fe_xNiGe$ and $MnNi_{1-x}Fe_xGe$) of the compound. This is due to the ferromagnetic coupling between the Fe and Mn spin-moments [10].

Sufficient amount of iron substitution has also been reported to induce a magnetostructural phase transition, form a PM, austenite parent phase to a FM, martensite low temperature phase [10]. A magnetostructural coupling like this should result in giant MCE, which is desirable for magnetic heat pump devices.

Clearly, the parent compound MnNiGe with $T_c = 470$ K and $T_N = 346$ K will not work in magnetic heat pump operated around RT. Different amounts of iron substitution may however couple the magnetic and structural transition ($T_c = T_n$) and allow tuning of the magnetostructural phase transitions towards room temperature, $T_c = T_n \approx RT$ [10]. This makes the intermetallic MnNiGe compound with Fe-substitution promising as a magnetocaloric material.

Chapter 3

Methodology

3.1 The instruments

3.1.1 The glove box

The UNIlab BRAUN glovebox contains a few mbar overpressure of argon. The inert gas is used in order to avoid reactions between samples and any molecules/particles in surrounding air. Humidity and oxygen levels are kept as low as possible, at around one ppm inside the box. The values are monitored and indicated by a digital display. An entering chamber is used when new samples or equipment is introduced to the box. Air is removed from the chamber by a vacuum pump and replaced with argon gas. The chamber is flushed with argon four to five times before exposed to the glove box environment.

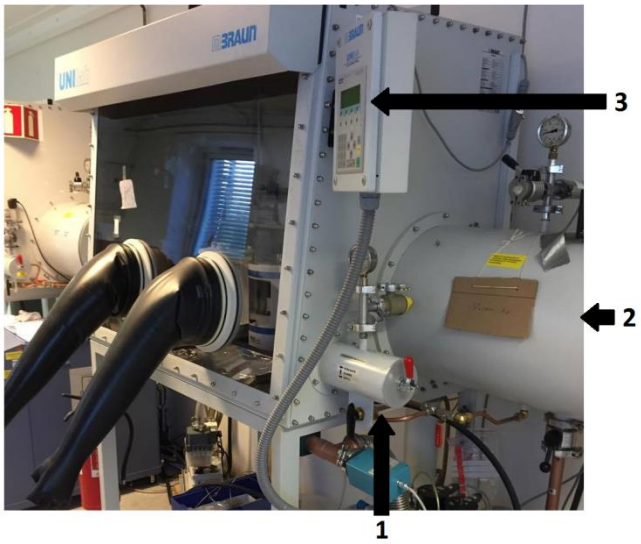

Figure 3.1: *The UNIlab BRAUN glove box with one small (arrow one) and one big (arrow two) entering chambers. The digital display monitor is shown by arrow three.*

3.1.2 The balances

The balances used for this experiment are a Mettler Toledo AG204 DeltaRange and a Sartorius ED124S Extend. The AG204 was used for balancing the right stoichiometric elemental amounts for each batch. These measurements were done inside the glove box. The Sartorius ED124S was used for measuring samples for the DSC experiments. Determining the exact uncertainty of the weight involve several factors. In the article 'Estimating Weighing Uncertainty From Balance Sheet Specifications', Arthur Reichmuth derives the normalized standard deviation of a balance as:

$$S = \sqrt{\frac{1}{m^2} * \left(SPC_{RP}{}^2 + \frac{2}{3} SPC_{NL}{}^2\right) + \frac{1}{3} * \left(SPC_{CAL,rel}{}^2 + \frac{1}{3}(SPC_{TCS} d_t)^2\right)} \quad \textbf{(3.1)}$$

where *S* is the standard deviation, *m* is the mass of the sample, *SPC* stands for specification, *RP* is the repeatability, *NL* is the non-linearity, *CAL,rel* is the relative calibration deviation, *TCS* is the temperature coefficient of sensitivity and d_t is the temperature deviation [30]. The uncertainty interval may further be calculated as:

$$U = K * S \quad \textbf{(3.2)}$$

where *K* is the confidence level expansion factor and *U* is the uncertainty interval. $K = 2$ results in a confidence interval of 95.45. Typical uncertainty values of weights like these (with $K = 2$), are 10^{-4} [30]. As this value is relative small, sample weight errors due to balance uncertainties are further neglected.

3.1.3 The electric arc furnace

The electric arc furnace is a device used for rapidly heating and cooling materials. The inside of this furnace consists of a sample holder crucible made of copper and a wolfram needle which is used to create the electric arc. The needle and sample holder are both mounted to metallic rods which extend into the volume of a thick surrounding glass dome. This is illustrated by the left side of figure 3.2. The dome can be sealed and filled with an inert gas like argon. Inert gases are used in order to avoid any reactions between the sample surface and molecules/particles in surrounding air. Air is removed by the use of a vacuum pump. This pump is controlled by a valve shown on the blue pipe line in figure 3.2. The argon supply is connected to the green pipe line. This connection is also controlled by an adjustable valve. The two rods inside the dome are connected to an adjustable power supply, shown by the red lines. This creates an open electric circuit as long as the rods do not touch each other. The rod with the wolfram needle attached has an isolated end pointing out through the sealed dome, which is made movable by hand. As the power supply is activated, it is thereby possible to create an arc upon moving the needle close to a sample loaded in the copper crucible. As the arc hits the sample, it will heat up to several thousand degrees Celsius. Afterwards it will cool down rapidly as cold water is continuously circulated through the copper crucible sample holder. The cooling cycle of the electric arc furnace is represented by the purple lines. Cold water is circulated through the sample holder by entering one end of the circuit and exiting the other.

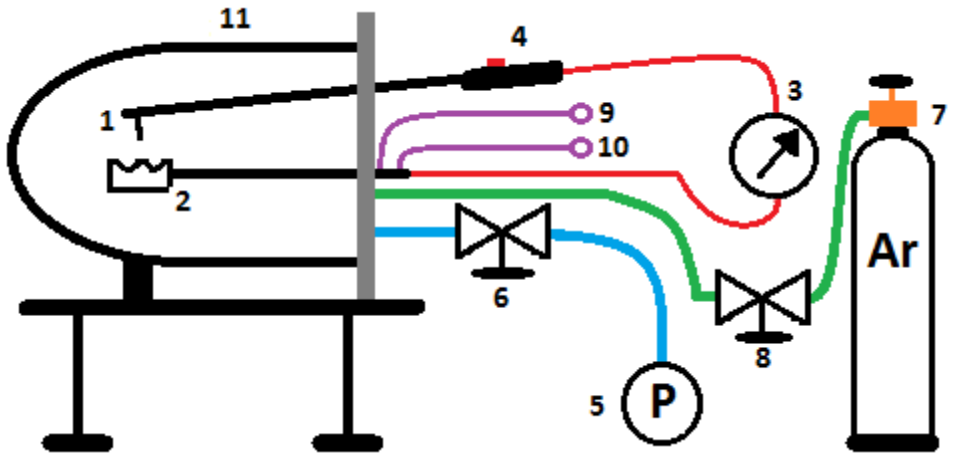

Figure 3.2: *The electric arc furnace system. The inside of the furnace is shown on the left side of the figure, containing a wolfram needle (1), a sample holder (2) and a thick glass dome (11). The right side of the figure shows the circulating systems of the furnace. The WECO Discovery 160T adjustable powers source (3) is connected to an isolated handle (4) with a connected red power button for activating the source. The Edwards RV12 oil filter pump (5) with the corresponding valve (6) evacuates the air, while the valve (8) connected to the argon tank (7) supplies the inert gas. The water cooling system has a water inlet (9) and outlet (10) connected directly to the sample holder, circulating water through the copper crucible.*

3.1.4 The pellet press

The PIKE crushIR at IFE is a hydraulic press used for making pellets out of powdered samples. The device consists of a hydraulic system, a digital display and a chamber for mounting a pellet die. The round pellet die has a hole with a given diameter where the sample may be loaded. Arrow one in figure 3.3 indicates where the die is placed inside the chamber. A piston is connected to the top part of the die and the bottom part of the press. The chamber is covered by a transparent safety shield. The hydraulic system is connected to a hand operated pump shown by arrow two in figure 3.3. The black wheel shown by arrow number three may be turned in order to release the hydraulic pressure. The amount of force needed in order to make an intact pellet is determined by the diameter of the pellet die and the type of materials in the sample. Pressure values are indicated in US tons by a digital display shown by arrow 4 in figure 3.3. This press is capable of reaching pressure values up to 15 US tons [36], which equals 13.6 metric tons. Arrow five shows a top wheel which adjusts the level of the press in order to take the die in or out.

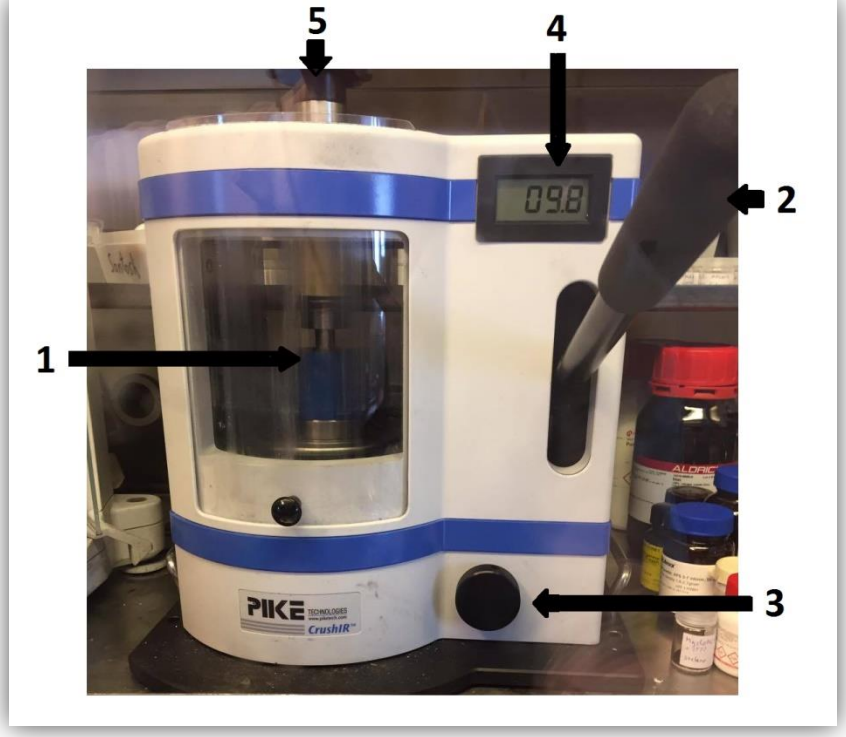

Figure 3.3: *The PIKE crushIR hydraulic press. Arrow one shows the pellet die placed inside the press. The hand operated pump for the hydraulic system is shown by arrow two, and the hydraulic pressure release/closure wheel is shown by arrow three. The digital display is shown in the top right by arrow four and the level adjustment wheel is shown by arrow five.*

3.1.5 The furnace

The Carbolite CWF 1100 muffle furnace is a high temperature electric furnace. The device consists of an isolated electric heated burning chamber and a digital display for adjusting and monitoring temperature. It can reach a temperature of 1100 ℃ [35]. A horizontal, electric tube furnace with the same working principle was also used.

3.1.6 The differential scanning calorimeter

The differential scanning calorimeter TA DSC25 Discovery is used for measuring temperatures and heat flow associated with material transitions. The core of the DSC is called the measuring cell and is illustrated by figure 3.4. This is where samples are loaded and temperatures are regulated and measured. A sample is loaded into the cell within a small aluminum pan sealed with a lid. The pan is placed on top of a sample platform. An equal empty pan which acts as a reference is placed on a second platform. Two platforms (illustrated by grey in figure 3.4.) are thermal conductive and connected to each other. The connected base area of the two platforms is temperature regulated and acts as the furnace of the system. Chromel within the sample platforms and the aluminum pans are both materials with high thermal conductivity. This means heat transfer from the furnace to the samples is achieved through conductivity. The furnace is cooled with liquid nitrogen and heated with electricity. This is illustrated by the squares 3 and 4 in figure 3.4. The TA DSC25 Discovery has a temperature range from -180 to +725 ℃ [31]. The measuring cell keeps track of the pan temperatures individually. Temperatures are not measured directly in the samples but at the sample platforms by a thermocouple. Due to conductivity it is further assumed that the pan-temperatures are equal to the platform temperatures ($T_s = T_1$ and $T_r = T_2$).

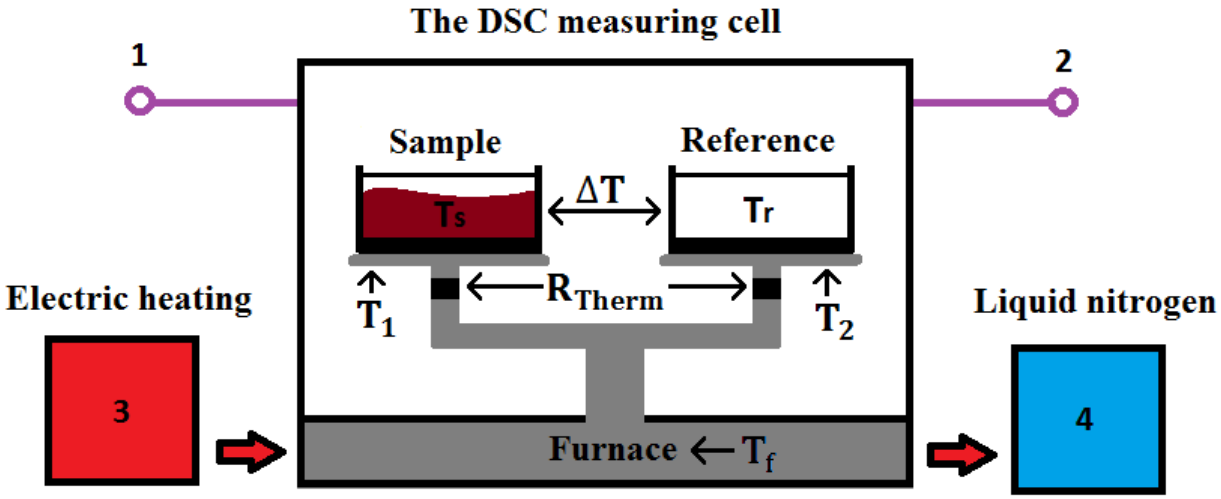

Figure 3.4: *A schematic drawing of the DSC measuring cell. An electric furnace is used for heating the system and liquid nitrogen is used for removing heat from the system. The sample in the left pan is indicated by brown and its associated temperature by T_s. The reference pan with its associated temperature T_r is shown on the right. The system has an inlet (1) and outlet (2) for helium flushing which is used to avoid condensation of oxygen and thereby contamination.*

When a constant heat flux is introduced by the furnace, the sealed pans will start to heat up. Due to different heat capacity in the sample and the reference pan, there will be a slight temperature difference between the two pans upon heating. As a phase transition occurs in the sample, the temperature of the sample pan (T_s) will stop increasing and stay constant until the transition is complete. Meanwhile, the temperature of the reference pan (T_r) continues to increase linearly. Thereby a phase transition may be indicated where the difference between T_r and T_s start to increase [31]. The heat flow (q) due to the temperature difference of the two pans ($\Delta T = T_r - T_s$) is calculated as:

$$q = \frac{T_r - T_s}{R_{\text{therm}}} \qquad \textbf{(3.3)}$$

Equation 3.3 is used under the assumption that the furnace temperature is uniformly distributed through the cell and that the thermal resistance (R_{therm}) through the two platforms and pans is equal [31]. By plotting the heat flow *q(T)* during a phase transition, temperatures and characteristics of a sample may be determined.

3.1.7 The X-ray diffractometer

The X-ray diffractometer used in this thesis is the BRUKER D8 Advance at IFE. The working principle of X-ray diffraction is described in detail in chapter 2.2.2. As shown in figure 3.5, the X-ray diffractometer consists of an X-ray source (1), an adjustable sample holder (2) and a detector (3). The X-rays hit the sample and scatter off to the detector. The sample is concealed in a glass capillary, which is mounted on the goniometer. The sample attached to the goniometer is mounted horizontally to the X-ray diffractometer. The sample is slowly rotated while the experiment is running to make sure all the atomic planes of the crystalline powder are hit with the right scattering angle at some point.

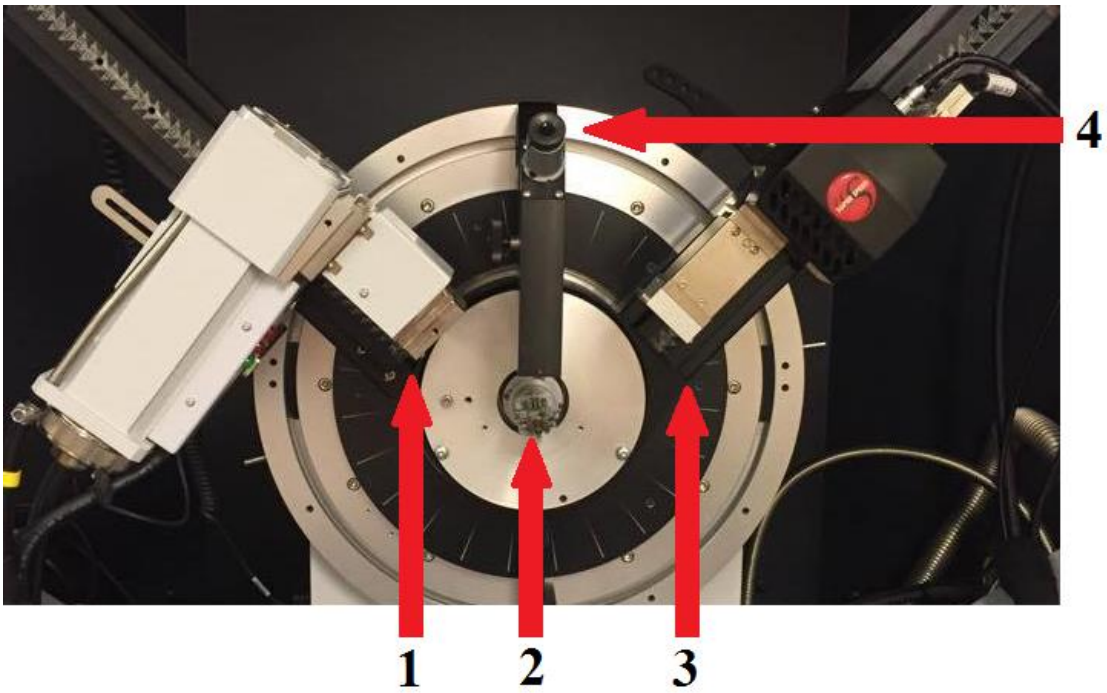

Figure 3.5: *The BRUKER D8 Advance X-ray diffractometer at IFE. Arrow one indicates the X-ray source. The goniometer holding the sample-capillary is mounted horizontally in front of the X-ray source and is shown by arrow two. The lynx-eye detector capturing scattered rays is shown by arrow three, and the microscope for adjusting the goniometer by arrow four.*

3.1.8 The Scanning electron microscope

A scanning electron microscope (SEM) scans a sample specimen by the use of electrons. Distinctive signals from electron-sample-interactions are detected and used to determine the sample morphology and composition [32]. The morphology is determined by secondary electrons due to ionization of surface atoms and backscattered electrons. The composition of a sample is determined by emitted X-rays from electron-excited atoms. The emitted X-rays are distinctive for different elements [33]. This type of component determination is called energy dispersive X-ray spectroscopy (EDS) analysis. Figure 3.6 illustrates the working principle of a SEM. For this thesis, the HITACHI scanning electron microscope at the University of Oslo was used.

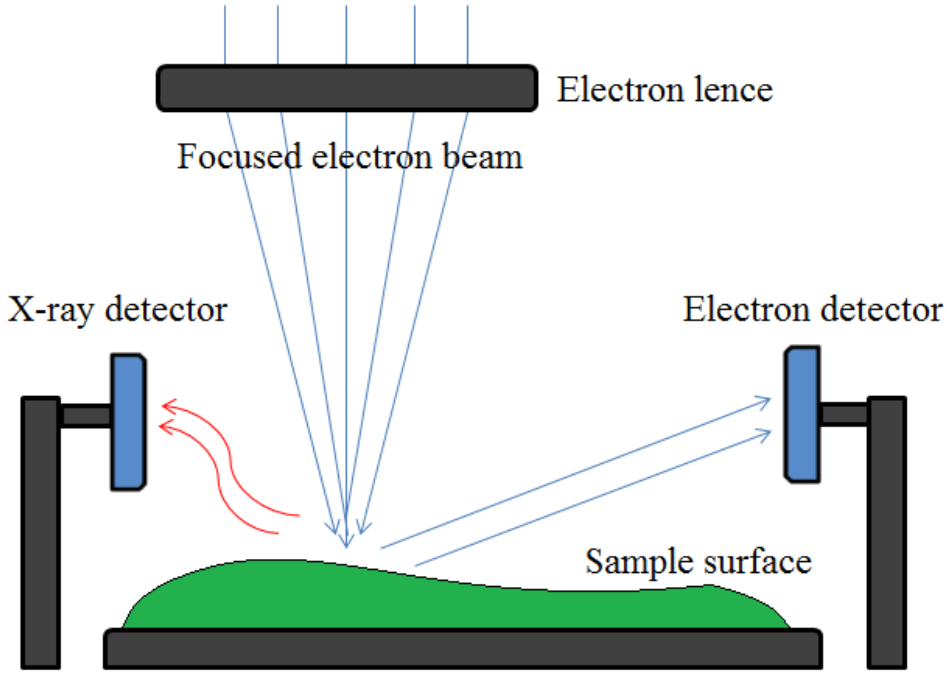

Figure 3.6: *The main components of a SEM. An electron lense focuses and accelerates electrons towards one point of the sample. Electron-sample-interactions result in scattered X-rays (red) and electrons (blue). Scattered rays are detected by two sensors, one X-ray detector and one electron detector. The focused electron beam will move and eventually scan the whole sample surface. Detector signals are then used to determine the morphology and elemental composition of the sample.*

3.1.9 The physical property measurement system

For magnetic measurements, the Quantum Design physical property measurement system (PPMS) at the University of Oslo was used. This device has a variable temperature-field system, designed to perform a variety of automated measurements. In this case, the magnetization of a sample is measured as temperature M(T) and external field M(H) variations are applied. The magnetization was determined using direct current magnetometry. This technique involves magnetizing a sample by an external field and moving it through a set of pic-up coils. Induced voltage in the coils due to Faraday's law may is measured and used to determine the magnetization of the sample [34].

3.1.10 The PUS high resolution diffractometer

A powder neutron diffraction experiment was performed at the PUS high resolution diffractometer in the JEEP II nuclear reactor at IFE. Just as for the X-ray diffractometer, the main components of this device are a radiation source, a sample holder (within a chamber) and a detector. Neutrons emitted form decaying Uranium 235 and its fission products within the JEEP II reactor core are used as the radiation source. The radiation is focused by a collimator towards a monochromator made of germanium, which reflects desired wavelengths further towards the sample. The sample chamber is temperature and pressure –regulated. After the sample is radiated, scattered neutrons pass through a second collimator (to remove noise) and hit a detector bank [18]. Two detector banks are air-hovered and moved around the sample in order to detect scattered neutrons at different angles. Each bank consists of seven stacked neutron detectors. These neutron detectors are tubes containing helium gas. The scattered neutrons are detected as they excite the gas within the tubes according to their wavelengths.

3.2 Procedure

3.2.1 Sample preparation

The right stoichiometric amounts for two grams of the intermetallic compounds $Mn_{1-x}Fe_xNiGe$ ($x = 0.03, 0.05, 0.07, 0.10, 0.15, 0.25$) and $MnNi_{1-x}Fe_xGe$ ($x = 0.05, 0.10, 0.15, 0.25$) were calculated. As Mn has a relative high vapor pressure, and additional four percent were added to compensate for evaporation. All the elements (Mn, Ni, Gr and Fe) were accessed as fine powder and weighted with the AG204 DeltaRange balance. The elements were mixed directly into small glass containers and sealed with a lid. All the samples were prepared inside the UNIab glove box. See appendix A for calculated and weighted elemental content of each sample.

The Intermetallic compounds were created by rapidly melting and cooling the mixed elements several times. This was done using the electric arc furnace. The furnace was cleaned with paper, alcohol and a Dremel polishing machine. Further a sample and solid titanium were loaded into two separate parts of the copper crucible. The glass dome was sealed, and evacuated with the EDWARDS RV12 oil filter vacuum pump. When the Edwards Pirani 502 pressure monitor indicated $5 * 10^{-2}$ mbar, the system was flushed with argon until the pressure reached 0.75 bar. The flushing was repeated five times in order to remove excess air molecules. The loaded titanium was melted prior to the sample in order to remove any excess oxygen in the system. Then the sample was melted, quenched and flipped four to five times.

After arc melting, the samples were crushed and grinded into fine powder. In order to create homogenous compounds, all samples were annealed at 800 ℃ for five days. This was done in the Carbolite CWF 1100 muffle furnace and a similar tube furnace. The samples were loaded into the furnace within a sealed quartz tube with a slight overpressure of argon gas. In order to isolate samples within the tube, sample pellets were made with the PIKE crushIR hydraulic press. 1.3 gram of sample material was loaded into a 13 mm die and was pressed by 9 metric tons for two minutes in order to make intact pellets. Then, the pellets were wrapped in tantalum and molybdenum foil and loaded into quarts tubes. The tubes were sealed by torch-melting. After five days of annealing the samples were quenched in order to preserve the crystal structure formed at high temperature. Quenching avoids any additional unwanted transition occurring. The rapid cooling was achieved by dropping the quartz tubes into a solution of cold H2O + NaCl.

3.2.2 X-ray and DSC scans

X-ray and DSC measurements were performed on all the eleven samples before and after the annealing process. For DSC measurements aluminum pans containing 30mg of powder were prepared. The pans were sealed with lids using a press. The reference pan and the one containing the sample were then loaded into the measuring cell. Measurements were done with heating and cooling rates of 10 K/min between -180 and 300 ℃. The experiment was controlled by the Trios software.

For X-ray measurements, a few milligram of sample were loaded into a glass capillary and sealed with glue. The capillaries were further mounted onto a goniometer with wax and a soldering iron. The axes on the goniometer were aligned and mounted into the D8 Advance X-ray diffractometer. Data were collected by the Difrac plus XRD commander software in a 2θ range of 15-90 degrees with a step size of 0.01 degrees and a collection time of 2s/step.

3.2.3 Scanning electron microscope analysis

For the scanning electron microscope (ESM) and energy dispersive X-ray spectroscopy (EDS) analysis, the two annealed samples $Mn_{0.85}Fe_{0.15}NiGe$ and $Mn_{0.95}Fe_{0.05}NiGe$ were chosen. These samples were chosen as they were believed to have different atomic structures according to the data from the DSC analysis. A conductive carbon tape was attached to an adjustable, flat sample holder. Then, a few milligram of fine sample powder were poured onto the tape and pressed down with a spoon. Excess powder not sticking to the tape was blown off with a high pressure air blower. Further the sample holder was mounted into the HITACHI SEM with the right adjusted height. As the SEM was loaded, a vacuum pump depressurized the sample chamber and sealed it. An external joystick was used to localize different areas of the powder sample. Data were analyzed with the Hitachi TM3000 and Quantax 70 software.

3.2.4 Magnetic measurements

For magnetic measurements, the two annealed samples $Mn_{0.85}Fe_{0.15}NiGe$ and $MnNi_{0.85}Fe_{0.15}Ge$ were chosen. For sample preparation 25-30 mg of fine sample powder was poured into small gelatin capsules. Further a few drops of glue were applied sealing and attaching the powder to one end of the gelatin capsule. These capsules were loaded into the physical property measurement system (PPMS). For the M(T) measurements, a temperature range of 40 to 350 K and a constant field of 1000 Oe was chosen. A big temperature span was set in order to localize magnetic transition-temperature points. The heating rate was set to 5 K/min with a 5 K increment measure. The M(H) measurement protocol was set to $H = [0,5.2500]$ tesla and $T = [120,220]$ K with a 5 K temperature interval. The parameters were set according to magnetic transitions observed in the M(T) data.

3.2.5 Neutron powder diffraction

In addition to the eleven samples, an additional three gram batch of $Mn_{0.85}Fe_{0.15}NiGe$ was arc melted and annealed for five days at $800\ ℃$. This sample was made for a powder neutron diffraction experiment. The experiment was performed in the JEEP II nuclear reactor at IFE. For the neutron experiment, a bigger sample batch was needed due to relative weak interactions between radiation and the sample, and also because the neutron radiation has a lower intensity than X-rays [M. H. Sørby, personal reference]. 2.52 g of sample were loaded into a 6 mm vanadium tube sample holder. Vanadium was used as the material does not interfere with sample-scattering. The sample holder was sealed with indium thread and a cylinder head attached with six screws. Further the sample holder was mounted inside a DISPLEX cryostat fitted with helium supply for cooling and a pump attached for vacuum. The sample was first measured at room temperature and afterwards cooled to 180 K in order to obtain data above and below the structural transition observed in the DSC data.

Chapter 4

Results and discussion

4.1 Differential scanning calorimetry analysis

4.1.1 The heat flow signals

Figure 4.1 and 4.2 shows the DSC heat flow signals of the as cast intermetallic compounds $Mn_{1-x}Fe_xNiGe$ and $MnNi_{1-x}Fe_xGe$ with varied Fe-substitution. The peaks show heat flow associated with phase transitions. Peaks with a negative heat flow indicate an endothermic transition and are associated with the martensite - austenite transition during heating of the material. The peaks with a positive heat flow indicate an exothermic transition and are associated with the reverse austenite – martensite transition during cooling of the material. The as cast samples show a trend where transition-temperatures are reduced as higher values of Fe-substitution are introduced. Most of the transition peaks are quite distinctive, but some are not. This may be due to inhomogeneities in the samples [C. Frommen, personal reference]. Boundary barriers caused by additional phases in the substance may disrupt an otherwise smooth phase transition. The $Mn_{0.75}Fe_{0.25}NiGe$ sample has no indicated phase transition in the temperature region between 93 and 573 K.

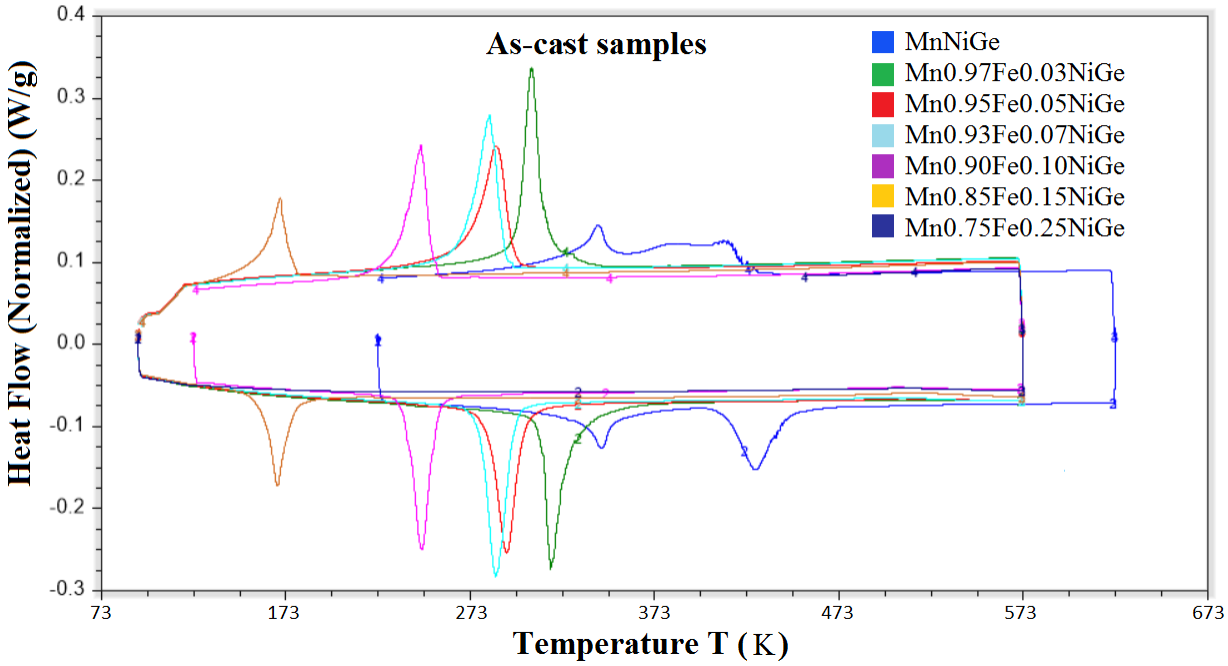

Figure 4.1: *The DSC heat flow signal from the as cast $Mn_{1-x}Fe_xNiGe$ compound with varied Fe-substitution ($x = 0, 0.03, 0.05, 0.07, 0.10, 0.15, 0.25$).*

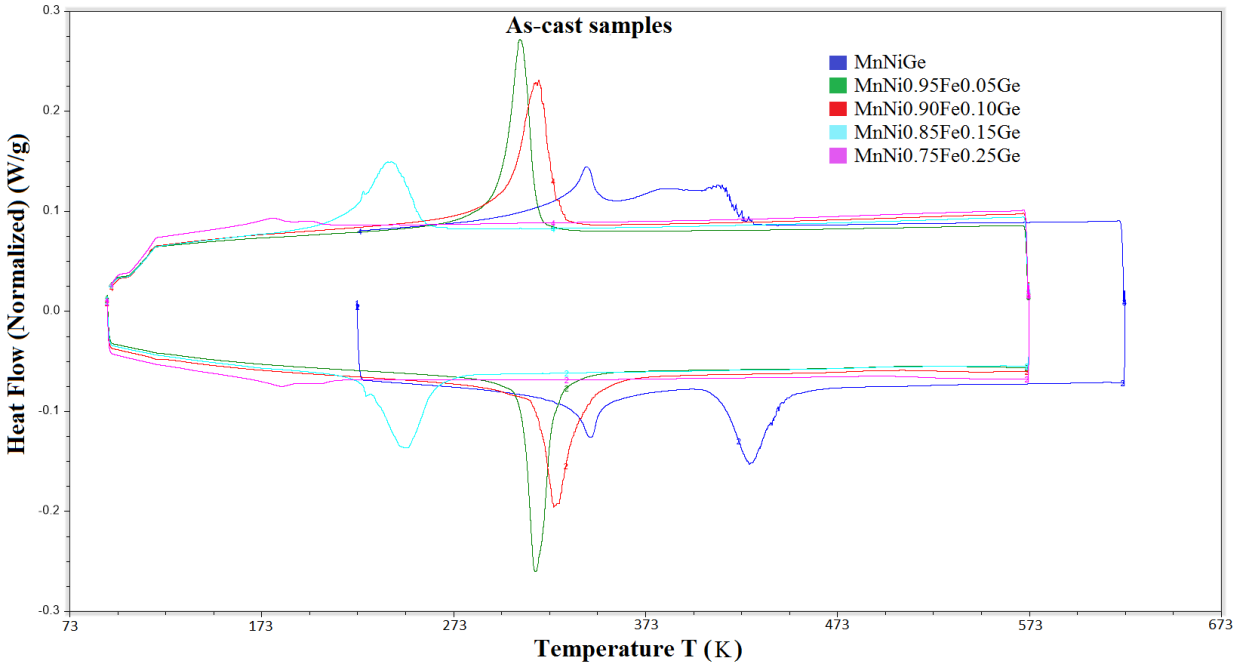

Figure 4.2: *The DSC heat flow signal from the as cast* $MnNi_{1-x}Fe_xGe$ *compound with varied Fe-substitution* ($x = 0, 0.05, 0.10, 0.15, 0.25$).

Figures 4.3 and 4.4 show the same samples after additional post-treatment (annealed for five days at 800 ℃). Just as for the as cast samples, the transition-temperatures are reduced as higher values of Fe-substitution are introduced. The annealed $Mn_{0.75}Fe_{0.25}NiGe$ sample has still no indicated phase transition in the temperature region between 93 and 573 K. This could mean the peak temperature occurs below 93 K.

Post-annealing has a clear influence on the phase transitions as all the peaks are more intense and sharper compared to the as cast state. The post-treatment could lead to an increased homogeneity in the combination with a reduced number of grain barriers in the samples. This in turn reduces the energy (temperature) needed to undergo the martensitic transition, hence the sharper and more pronounced peaks.

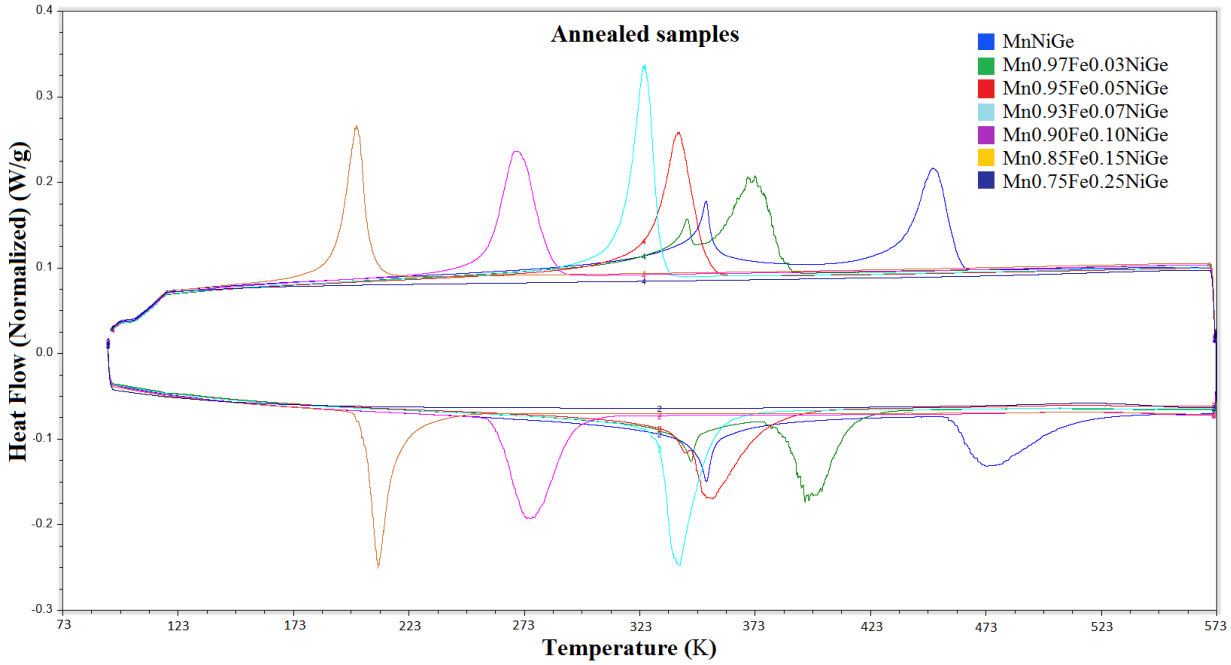

Figure 4.3: *The* $Mn_{1-x}Fe_xNiGe$ *compound with Fe-substitution* $x = 0, 0.03, 0.05, 0.07, 0.10, 0.15, 0.25$ *annealed for five days at* 800℃.

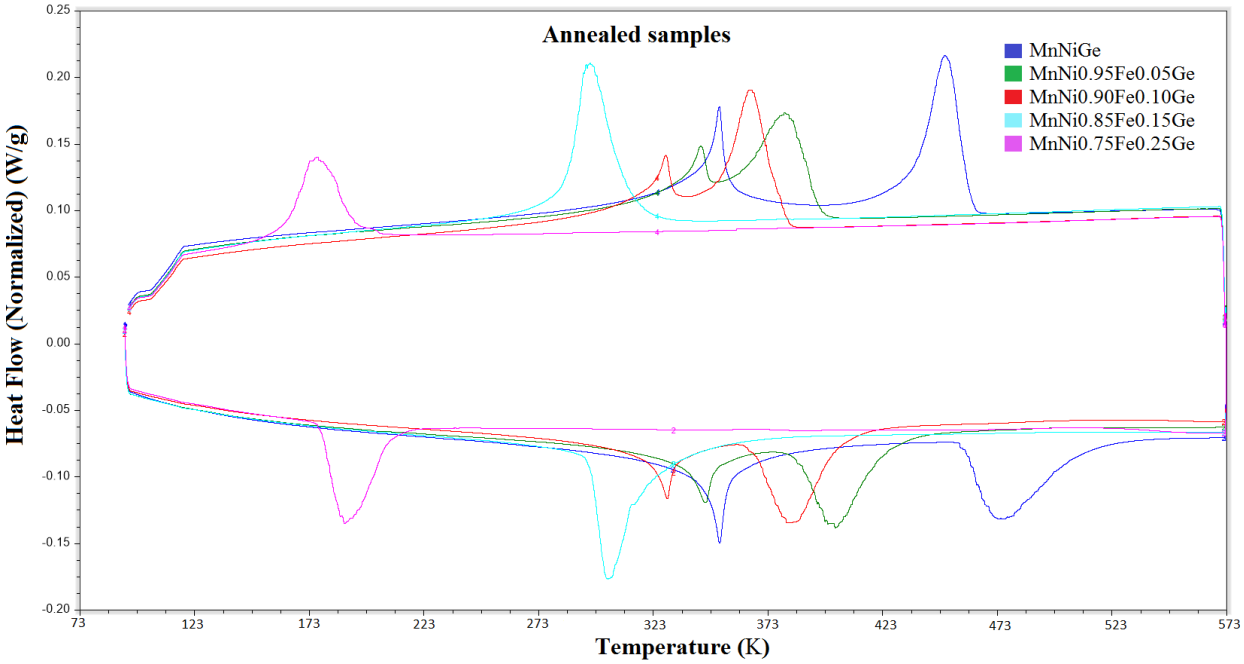

Figure 4.4: *The* $MnNi_{1-x}Fe_xGe$ *compounds with Fe-substitution* $x = 0, 0.05, 0.10, 0.15, 0.25$ *annealed for five days at* 800℃.

The broadness, shape and hysteresis associated with a transition peak give an indication of the transition-type. Let's take a look at the annealed MnNiGe compound. The sample shows two transition peaks in the given temperature span. The transition initiated at 465.4 K upon cooling have a large peak with transition-temperature span (22.9 K). It also shows large hysteresis (18.3 K). The relative large peak and clear hysteresis indicate the firs order nature of a martensitic structural transition. This thermal hysteresis is associated with the latent heat of the martensitic transition. The second peak, initiated at 356.6 K upon cooling is relative sharp and has a narrow transition-temperature span (6.86 K) and no apparent hysteresis. This peak is the result of a magnetic transition from a paramagnetic to a spiral antiferromagnetic state. Other research on the MnNiGe compound reports a PM-AFM transition initiated at $T_N = 346$ K and a martensitic transition initiated at $T_{mar.} = 470$ K upon heating [8]. This confirms the martensitic structural transition and the PM-AFM magnetic transition observed in the sample.

As small amounts of iron (three percent on the Mn site and ten percent on the Ni site) are introduced, the structural transition-temperatures are significantly reduced and moved closer to the magnetic transition-temperature. As higher values of Fe-substitutions are introduced, the magnetic transition peak seems to disappear. This could indicate that the magnetic and structural transitions occur at the same temperature point resulting in a magnetostructural coupling. However, there is no way of confirming the existence of a coupled magnetostructural transition by DSC alone, thus further analysis of the structural and magnetic properties of the samples is needed.

4.1.2 Transition span and hysteresis

Table 4.1 shows the structural transition-temperatures of the annealed samples. For the eleven compounds, start and finishing temperatures of the martensite-austenite transition (upon heating) are listed as $T_{\mathrm{aust(start)}}$ and $T_{\mathrm{aust(finish)}}$. The start and finishing temperatures of the austenite-martensite transition (upon cooling) are also listed and denoted $T_{\mathrm{mart(start)}}$ and $T_{\mathrm{mart(finish)}}$. The temperature span of the heating and cooling transitions are further calculated and listed as $T_{\mathrm{span(aust)}}$ and $T_{\mathrm{span(mart)}}$. The temperature spans are quite broad. This indicates a persisting martensitic transition.

Table 4.1: *The martensitic phase transition start and finishing temperatures of the annealed samples. The table also shows temperature spans of the structural transitions.*

Compound	$T_{\mathbf{aust(start)}}$ (K)	$T_{\mathbf{aust(finish)}}$ (K)	$T_{\mathbf{mart(start)}}$ (K)	$T_{\mathbf{mart(finish)}}$ (K)	$T_{\mathbf{span(aust)}}$ (K)	$T_{\mathbf{span(mart)}}$ (K)
MnNiGe	460.71	483.79	465.42	442.5	23.08	22.92
Mn0.97Fe0.03NiGe	385.79	405.82	380.72	363.22	20.03	17.5
Mn0.95Fe0.05NiGe	345.58	361.78	351.76	330	16.2	21.76
Mn0.93Fe0.07NiGe	331.84	348.56	332.44	318.05	16.72	14.39
Mn0.90Fe0.10NiGe	260.88	289.02	284.14	261.98	28.14	22.16
Mn0.85Fe0.15NiGe	203.42	215.42	207.04	194.58	12	12.46
Mn0.75Fe0.25NiGe	-	-	-	-	-	-
MnNi0.95Fe0.05Ge	387.89	410.1	394.65	372.69	22.21	21.96
MnNi0.90Fe0.10Ge	367.07	400.48	378.49	359.55	33.41	18.94
MnNi0.85Fe0.15Ge	295.75	323.79	316.26	287.71	28.04	28.55
MnNi0.75Fe0.25Ge	178.3	207.48	194.47	166.9	29.18	27.57

Table 4.2 shows calculated hysteresis associated with the two transitions of a sample, the one occurring upon heating and the one upon cooling ($\Delta T_{hyst(1)}$ and $\Delta T_{hyst(2)}$). The hysteresis is believed to have both thermal and magnetic contributions, if a MST is established. The hysteresis indicates how much energy will be lost in a magnetic heat pump device due to remaining material heat after one transition cycle. This has to be compensated by a larger magnetic field, which ultimately results in a lower efficiency. The compounds $Mn_{0.90}Fe_{0.10}NiGe$ and $MnNi_{0.85}Fe_{0.15}Ge$ show a significantly lower hysteresis than others. As both samples have martensitic transitions near room temperature, a change between the martensite and austenite structural phase will not require a lot of energy [C. Frommen, personal reference]. This could cause the reduction of hysteresis.

Table 4.2: *The calculated hysteresis associated with the structural and magnetostructural phase transitions.*

Compound	$\Delta T_{\mathbf{hyst\ (1)}}$ (K) $[T_{\mathbf{aust(start)}} - T_{\mathbf{mart(finish)}}]$	$\Delta T_{\mathbf{hyst\ (2)}}$ (K) $[T_{\mathbf{aust(finish)}} - T_{\mathbf{mart(start)}}]$
MnNiGe	18.21	18.37
Mn0.97Fe0.03NiGe	22.57	25.1
Mn0.95Fe0.05NiGe	15.58	10.02
Mn0.93Fe0.07NiGe	13.79	16.12
Mn0.90Fe0.10NiGe	-1.1	4.88
Mn0.85Fe0.15NiGe	8.84	8.38
Mn0.75Fe0.25NiGe	-	-
MnNi0.95Fe0.05Ge	15.2	15.45
MnNi0.90Fe0.10Ge	7.52	21.99
MnNi0.85Fe0.15Ge	8.04	7.53
MnNi0.75Fe0.25Ge	11.4	13.01

4.2 X-ray diffraction

4.2.1 The X-ray diffraction peaks

Figures 4.5 and 4.6 show the intensity of scattered X-rays plotted against the scattering angle 2θ. The values are measured at room temperature. For the $Mn_{1-x}Fe_xNiGe$ samples (figure 4.5) with zero to seven percent Fe-substitution, the Bragg peak positions fit an orthorhombic crystal structure. In addition to this parent phase, some impurities are observed. In the MnNiGe sample an additional tiny amount MnNiGe existing in a hexagonal phase is observed. Also, a tiny additional hexagonal Fe_2Ge phase is observed in the $Mn_{0.95}Fe_{0.15}NiGe$ sample. The 10 to 25 percent Fe-substituted samples appear to have a pure hexagonal MnNiGe crystal structure. The symbol *h* represents peak positions fitting a hexagonal diffraction pattern. The different positions of *h* are associated with different miller indices. The data fits well with the DSC results and the reported structural martensitic transition of the compound.

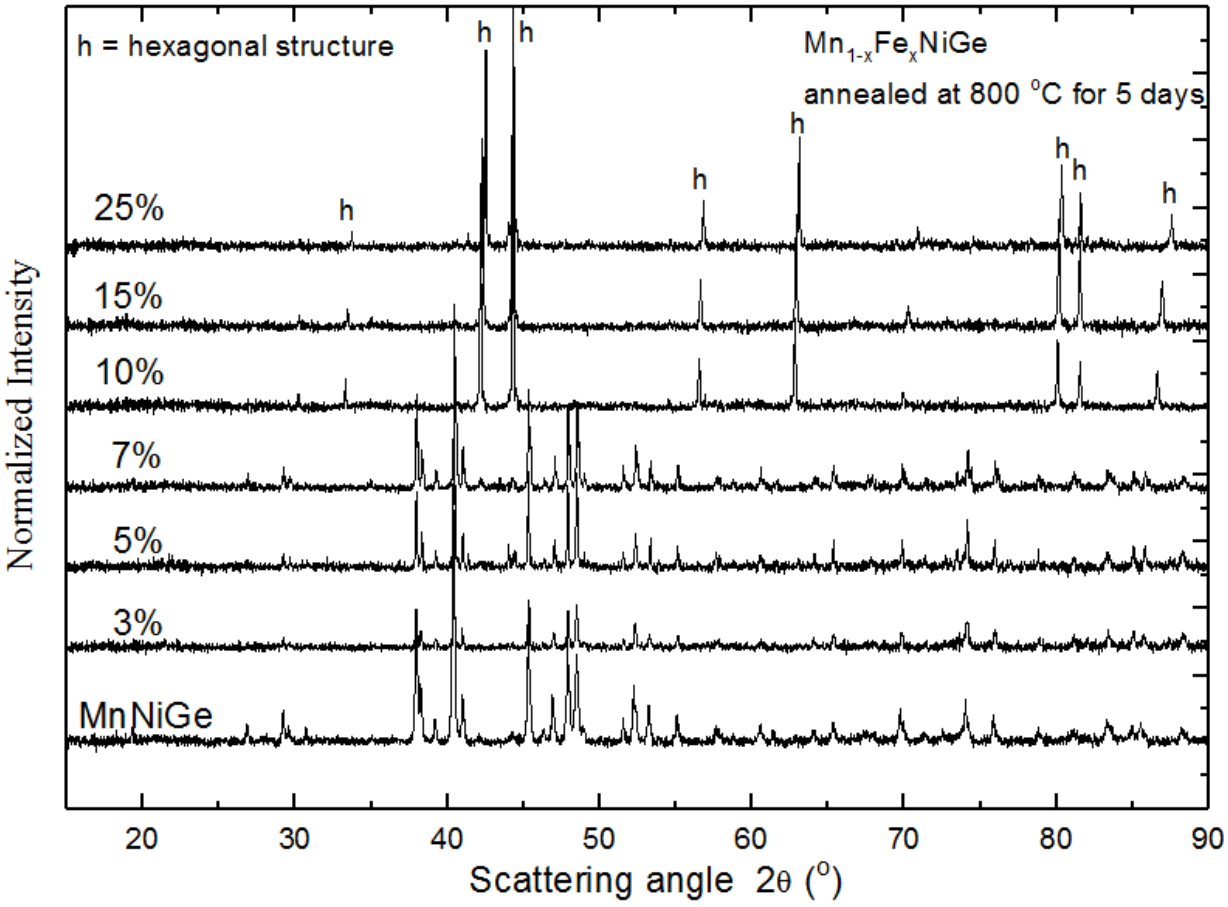

Figure 4.5: *The room temperature diffraction patterns of the annealed* $Mn_{1-x}Fe_xNiGe$ *compounds with Fe-substitution* $x = 0, 0.03, 0.05, 0.07, 0.10, 0.15, 0.25$.

Figure 4.6 shows the X-ray powder patterns for a series of $MnNi_{1-x}Fe_xGe$ samples measured at RT. The samples with zero to ten percent Fe-substitution have a diffraction pattern fitting an orthorhombic crystal structure. Figure 4.7 compares powder diffraction peaks of the $MnNi_{0.85}Fe_{0.15}$ sample to the hexagonal $Mn_{0.85}Fe_{0.15}NiGe$ sample. $MnNi_{0.85}Fe_{0.15}$ appears to have a mixed state equally represented by a hexagonal and orthorhombic phase. The DSC data reports a structural transition-temperature close to RT (see figure 4.4). This could explain why the sample exists in such a mixed sate. The $MnNi_{0.75}Fe_{0.25}Ge$ shows a pure hexagonal phase. Just as for the $Mn_{0.95}Fe_{0.15}NiGe$ sample, a tiny Fe_2Ge hexagonal phase is found in the $MnNi_{0.95}Fe0.05$ and $MnNi_{0.85}Fe_{0.15}$ samples. This could be a result of the casting process, where a binary Fe_2Ge phase has formed instead of the MnFeNiGe due to slightly different experimental conditions. Metallurgy is a complicated field. Even with optimal condition it can be difficult to obtain single phase materials [C. Frommen, personal reference].

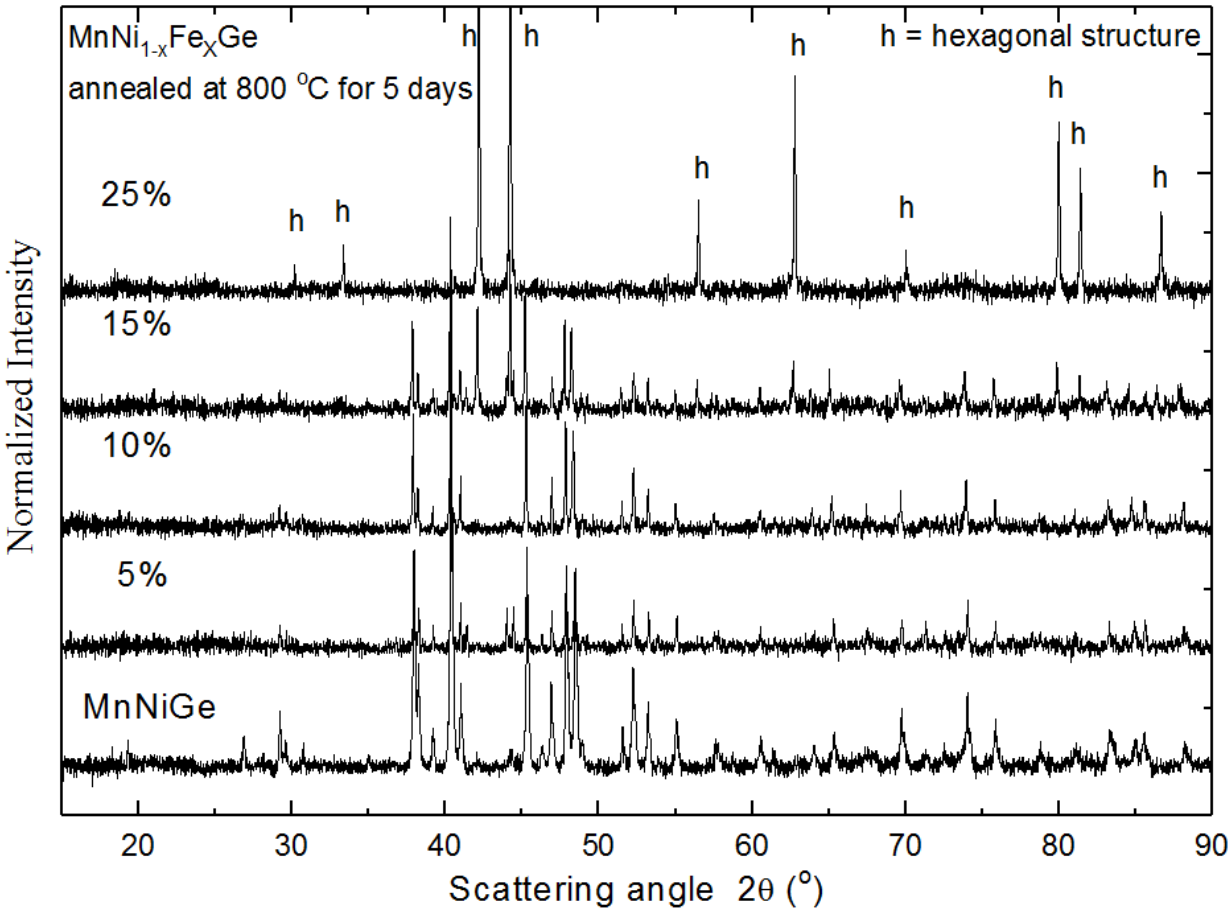

Figure 4.6: *The room temperature diffraction patterns of the annealed* $MnNi_{1-x}Fe_xGe$ *compounds with Fe-substitution* $x = 0, 0.05, 0.10, 0.15, 0.25$.

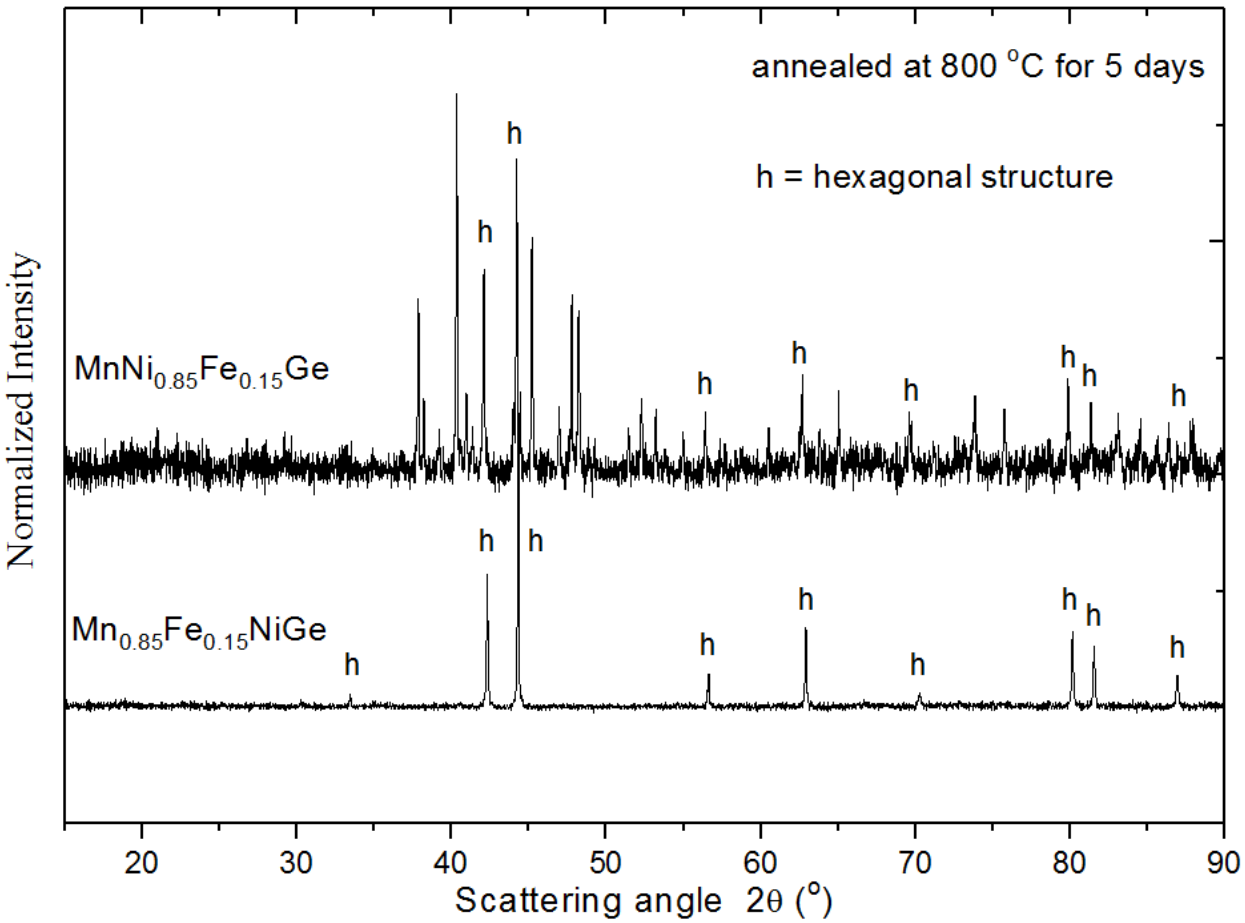

Figure 4.7: *A comparative plot of the diffraction patterns of the annealed* $MnNi_{0.85}Fe_{0.15}Ge$ *and* $Mn_{0.85}Fe_{0.15}NiGe$ *samples measured at room temperature.*

XRD data confirms the two reported structural phases of the compound. Sufficient amount of Fe-substitution appears to transform the hexagonal (austenite) phase into an orthorhombic (martensite) phase at RT. It appears that higher values of Fe-substitution on the Ni site (25 percent) is needed than on the Mn site (ten percent) in order for the compound to exist in a hexagonal state at RT. Fe-substitution on the Mn site has a more profound effect on the martensitic transition-temperatures than on the Ni site and less Fe is needed to bring the transitions temperatures towards room temperature.

4.2.2 Refined lattice parameters

Figure 4.8 shows the refined lattice parameters of the $Mn_{1-x}Fe_xNiGe$ compound at RT. The hexagonal austenite parent phase is introduced at ten percent iron substitution. The calculated average volume of the orthorhombic and hexagonal unit cell is 160.32 Å^3 and 89.39 Å^3, which gives a volume change of $\Delta V = 70.92$ Å^3. It is difficult to see any effect on the lattice parameters apart from the structural transition from this plot, but high resolution parameter data (listed in Appendix B), indicates a trend of decreasing *a* with increasing iron content. This is the case of both the orthorhombic and hexagonal phase. Lattice parameter *b* and *c* does not indicate any trends apart from the martensitic structural transition. The crystal symmetry of the orthorhombic phase fits *P nma* pace group, and the crystal symmetry of the hexagonal phase fits a $P\ 6_3/mmc$ space group

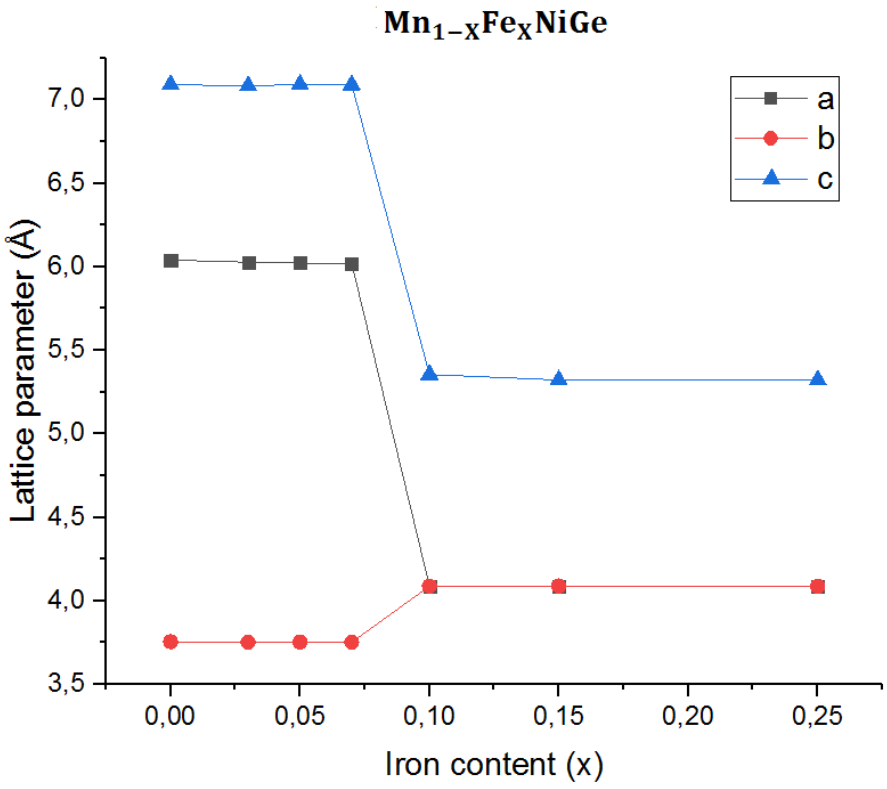

Figure 4.8: *The lattice parameters of the annealed $MnNi_{1-x}Fe_xGe$ compound with varied iron content at RT.*

Figure 4.9 shows the refined lattice parameters of the $MnNi_{1-x}Fe_xGe$ compound. Little change in the lattice parameters is observed until the hexagonal phase is introduced at $x > 0.15$, but an equal trend of decreasing *a* is indicated (see Appendix B). At $x = 0.15$, the crystal structure coexists in an orthorhombic and hexagonal phase. The calculated average volume of the orthorhombic and hexagonal unit cell is 161.18 Å^3 and 90.085 Å^3, which gives a volume change of $\Delta V =$ 71.095 Å^3. Just as for the $Mn_{1-x}Fe_xNiGe$ compounds, the crystal symmetry of the orthorhombic phase fits a *P nma* pace group, and the crystal symmetri of the hexagonal phase fits a *P* $6_3/mmc$ space group

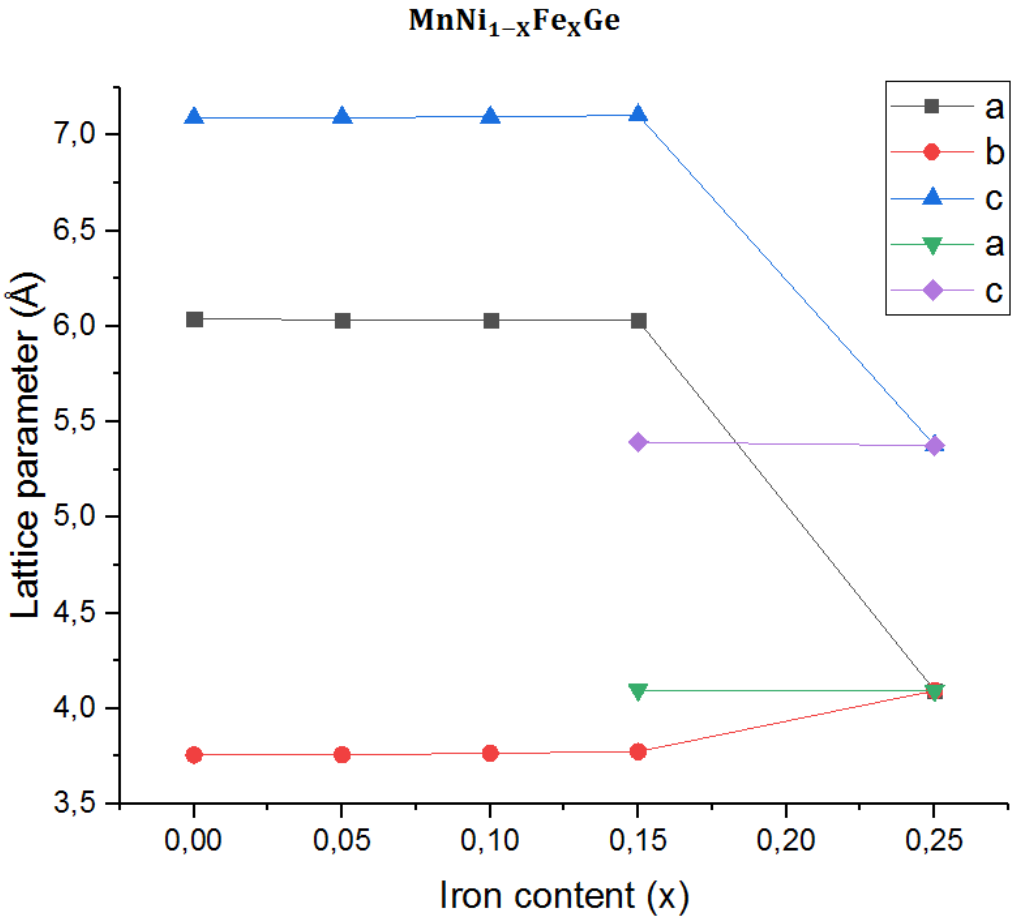

Figure 4.9: *The lattice parameters of the annealed $Mn_{1-x}Fe_xNiGe$ compound with varied iron content at RT.*

4.3 Neutron diffraction analysis

4.3.1 Neutron diffraction powder patterns

Figure 4.10 shows the powder neutron experiment (PND) data from the PUS high resolution diffractometer. The intensity of scattered neutrons is plotted against 2θ at RT and 180 K. X-ray diffraction and DSC data indicated the $Mn_{0.85}Fe_{0.15}NiGe$ sample existing in a hexagonal state at RT. A refinement of the $Mn_{0.85}Fe_{0.15}NiGe$ neutron diffraction pattern confirms this pure hexagonal crystal structure with space group $P\ 6_3/mmc$. It was not enough time to refine the 180K data, but the plots confirm an establishment of a lower symmetric (orthorhombic) crystal structure.

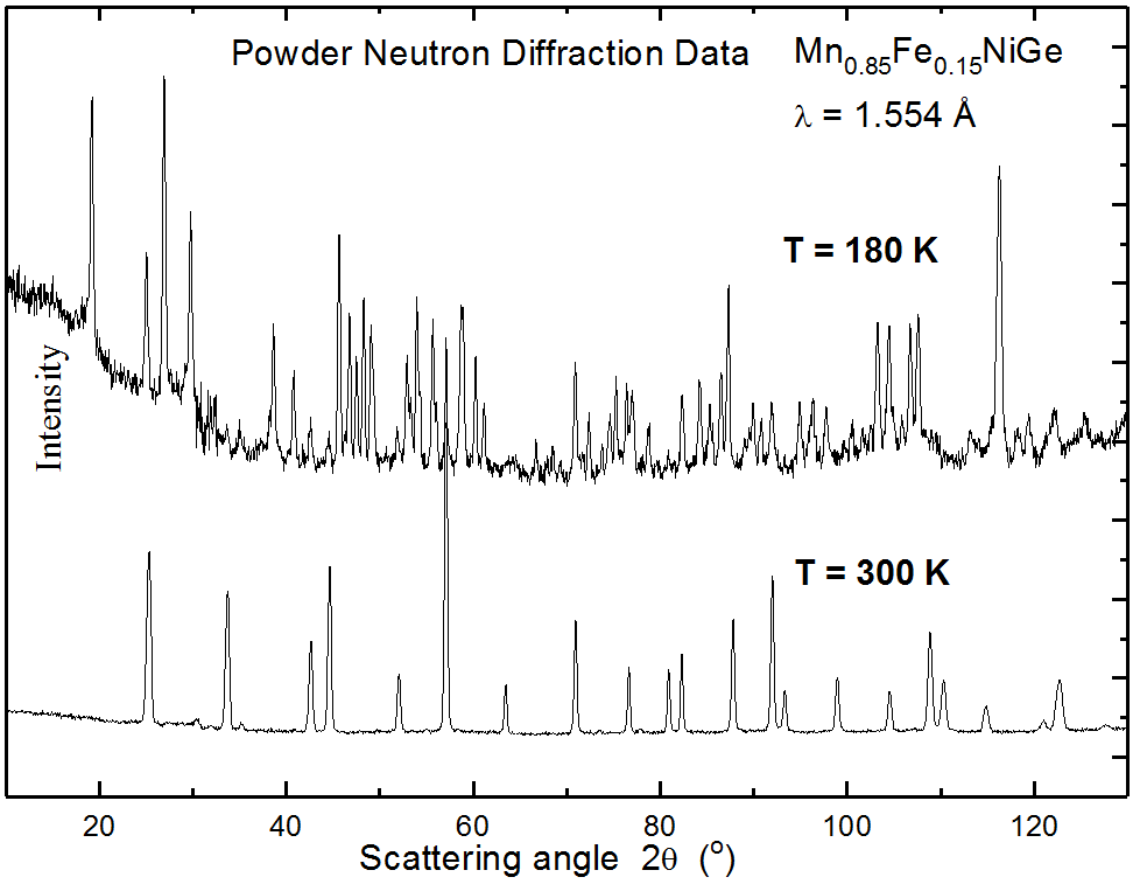

Figure 4.10: *Neutron diffraction patterns of the $Mn_{0.85}Fe_{0.15}NiGe$ at 300 and 180 K.*

4.3.2 Neutron data refinement

A refinement of the RT $Mn_{0.85}Fe_{0.15}NiGe$ powder diffraction peaks is shown by figure 4.11. The plot shows scattered radiation (neutrons) intensities as a function of 2θ. The pink bars indicate where the peaks of a hexagonal crystal structure should occur according to a crystallographic database. The x'es indicates observed data points and the red line indicates the estimated data points for a hexagonal crystal structure. The blue graph shows the difference between estimated and observed diffraction data.

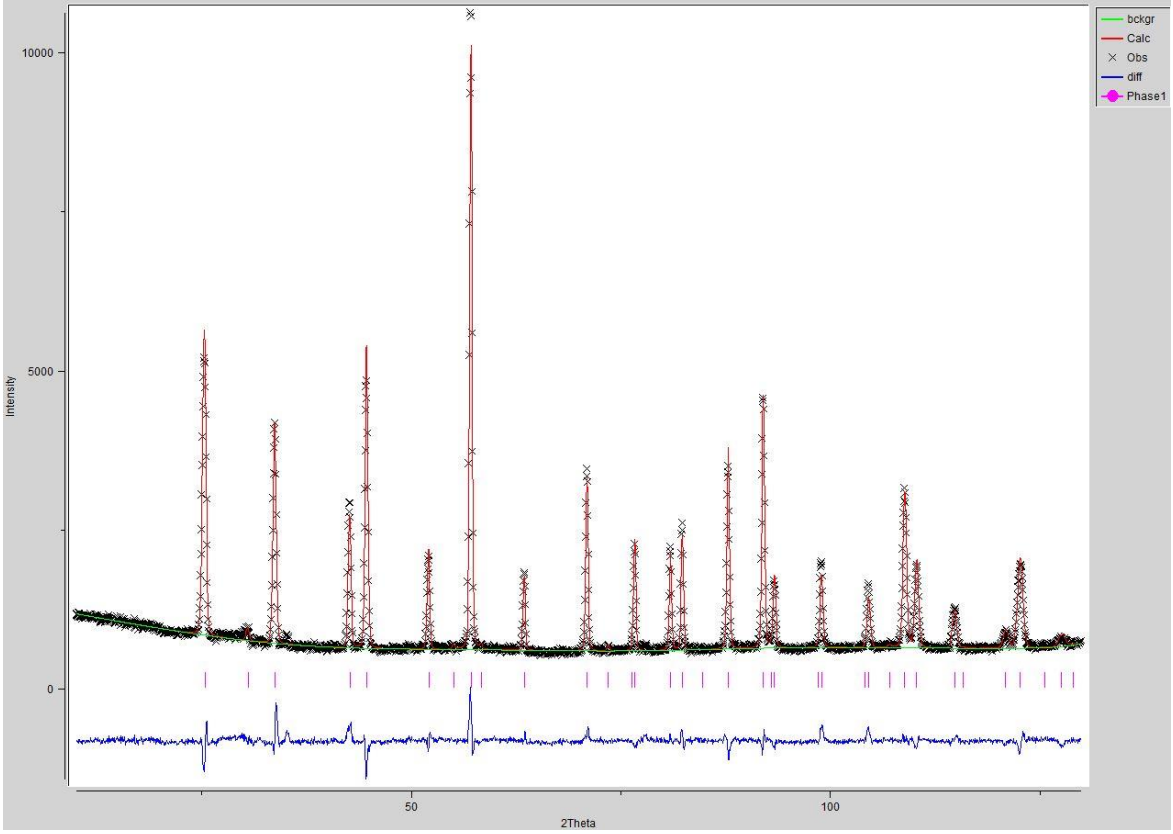

Figure 4.11: *Refinement of the $Mn_{0.85}Fe_{0.15}NiGe$ powder diffraction peaks at RT. The refinement was performed using the EXPGUI software.*

The refined lattices parameters of the RT sample is $a = 4.09$ Å, $b = 4.0905$ Å, $c = 5.3594$ Å, $\alpha = \beta = 90°$ and $\gamma = 120°$. This gives a unit cell volume of 89.674 Å3. X-ray diffraction refinement indicated an average unit cell volume of 89.39 $Å^3$. This confirms the reliability of the X-ray diffraction data and the structural determination of the compounds.

Although the Mn and Fe element has approximately the same atomic weight, they have distinctive neutron interactions. This makes it possible to refine the Mn/Fe occupancies of the sample. The refined occupancies indicate a 15.9 percent Fe-substitution in the Mn site. This this is quite close to EDS analysis results, which indicated an average of 14.2 Fe-substitution in the $Mn_{0.85}Fe_{0.15}NiGe$ sample.

Table 4.3: *Refined occupancies of the* $Mn_{0.85}Fe_{0.15}NiGe$ *sample*

Atom	Occupancy
Mn	0.841
Fe	0.159
Ni	1.0
Ge	1.0

4.4 Scanning electron microscopy

4.4.1 Investigation of powder morphology

Figures 4.12 and 4.13 show pictures of $Mn_{0.85}Fe_{0.15}NiGe$ and $Mn_{0.95}Fe_{0.05}NiGe$ crystallites taken by the scanning electron microscope. With a 400x magnification, one can see the surface and edges of crystallites. The $Mn_{0.85}Fe_{0.15}NiGe$ powder seems to have mostly intact surfaces with sharp edges. The $Mn_{0.85}Fe_{0.15}NiGe$ powder on the other hand, appears to have bubbly and cracked surfaces. The differences could be due to the crystal structures of the two samples. XRD data indicates the $Mn_{0.85}Fe_{0.15}NiGe$ sample having an orthorhombic crystal structure at RT. The $Mn_{0.95}Fe_{0.05}NiGe$ sample has an hexagonal crystal structure indicated at RT. Expansion of approximately 71 $Å^3$ per unit cell could crack the $Mn_{0.95}Fe_{0.05}NiGe$ crystallites upon cooling past the structural transition-temperature T_{mart} towards RT.

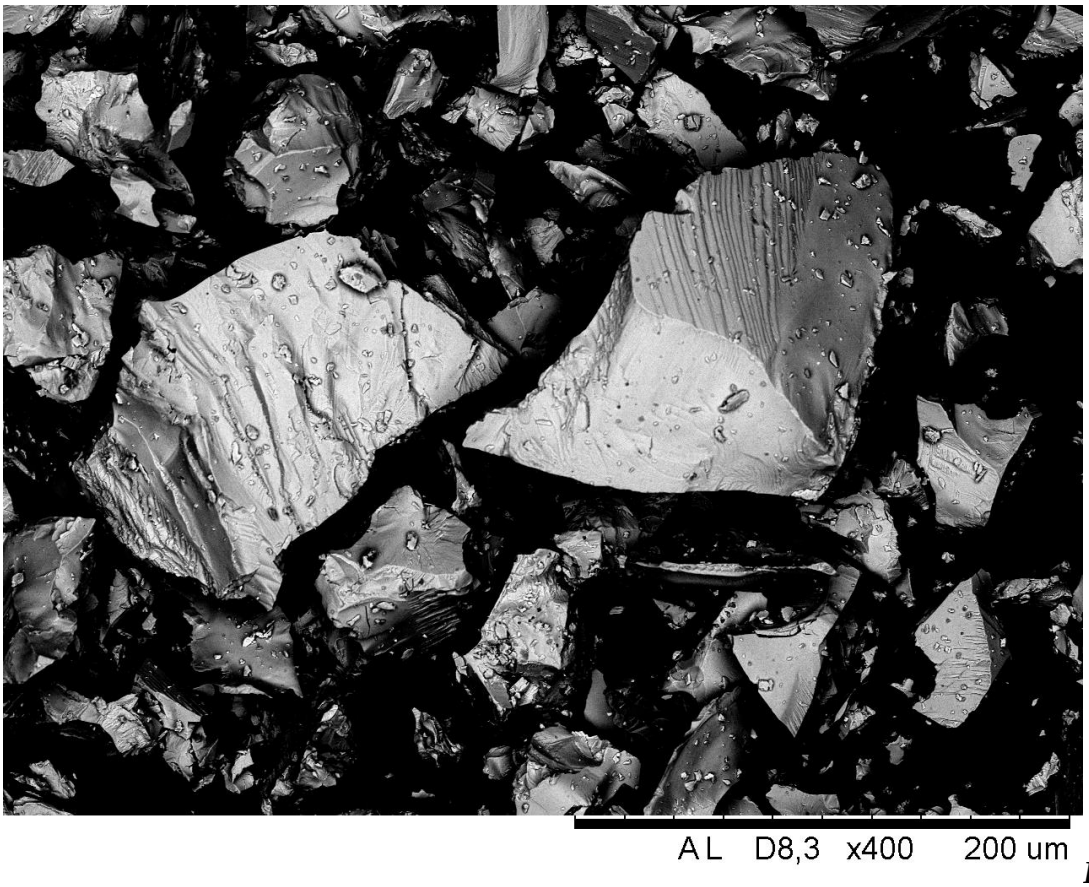

Figure 4.12: *The morphology of some $Mn_{0.85}Fe_{0.15}NiGe$ crystalites. The scanning electron microscope picture is taken with a 400x magnification.*

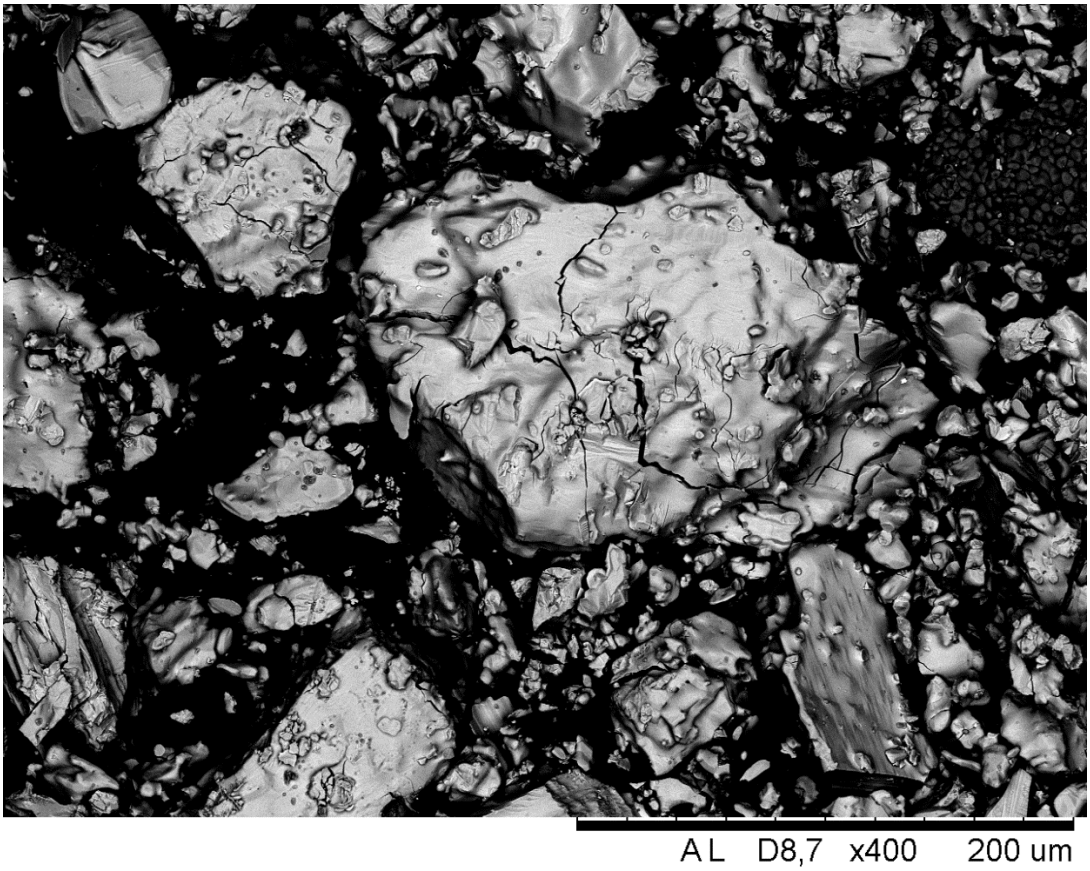

Figure 4.13: *The morphology of some $Mn_{0.95}Fe_{0.05}NiGe$ crystalites. The scanning electron microscope picture is taken with a 400x magnification.*

4.5 Energy dispersive X-ray spectroscopy (EDS)

4.5.1 An overview of the $Mn_{0.95}Fe_{0.05}NiGe$ sample

For the EDS analysis, firstly an overview picture of the $Mn_{0.95}Fe_{0.05}NiGe$ crystallites with a magnification factor of 400x was taken. Figure 4.14 shows the powder region selected for analysis. An EDS analysis was further run. The blue, yellow, purple and orange pictures in figure 4.14 shows the Ni, Ge, Mn and Fe content of the crystallite surfaces. Bright spots represent high elemental content and dark spots represent low elemental content. The associated photon energies and intensities emitted from the selected region is plotted in figure 4.15.The total elemental distribution is shown by the lower left picture in figure 4.14. This picture indicates a quite homogenously distributed elemental content of the crystallites. There are some regions where no or little content is shown. These areas are the same for all the elemental pictures and are due to uneven sample surface or absence of crystals. Rough surface areas could lead to emitted X-ray distortions and X-rays emitted away from the detector. This is why flat crystallite surfaces are preferred for EDS analysis and chosen for further elemental content determination.

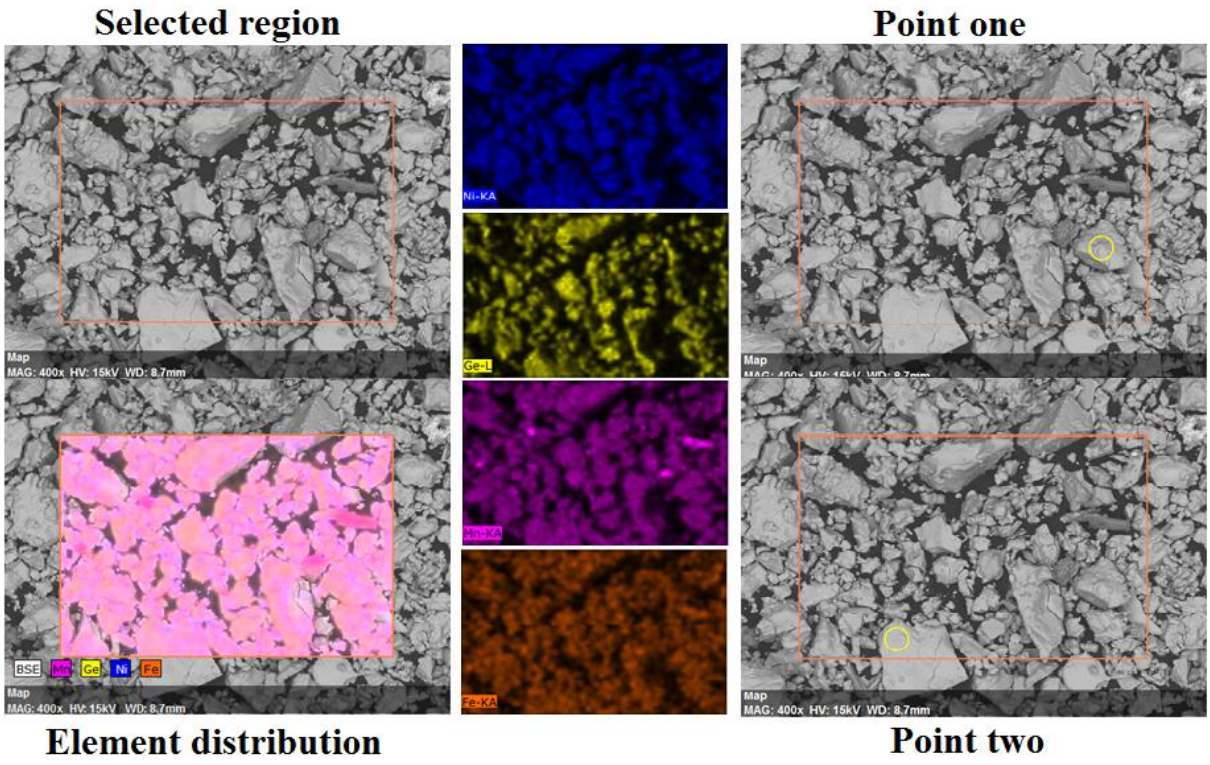

Figure 4.14: *An overview of $Mn_{0.95}Fe_{0.05}NiGe$ crystallites. The blue, yellow, purple and orange pictures represent the Ni, Ge, Mn and Fe content of the crystallite surfaces. Bright spots indicate high elemental content and dark spots indicate low elemental content. The two flat surfaces (point one and two) are selected for accurate elemental content determination. The picture was taken with a magnification factor of 400.*

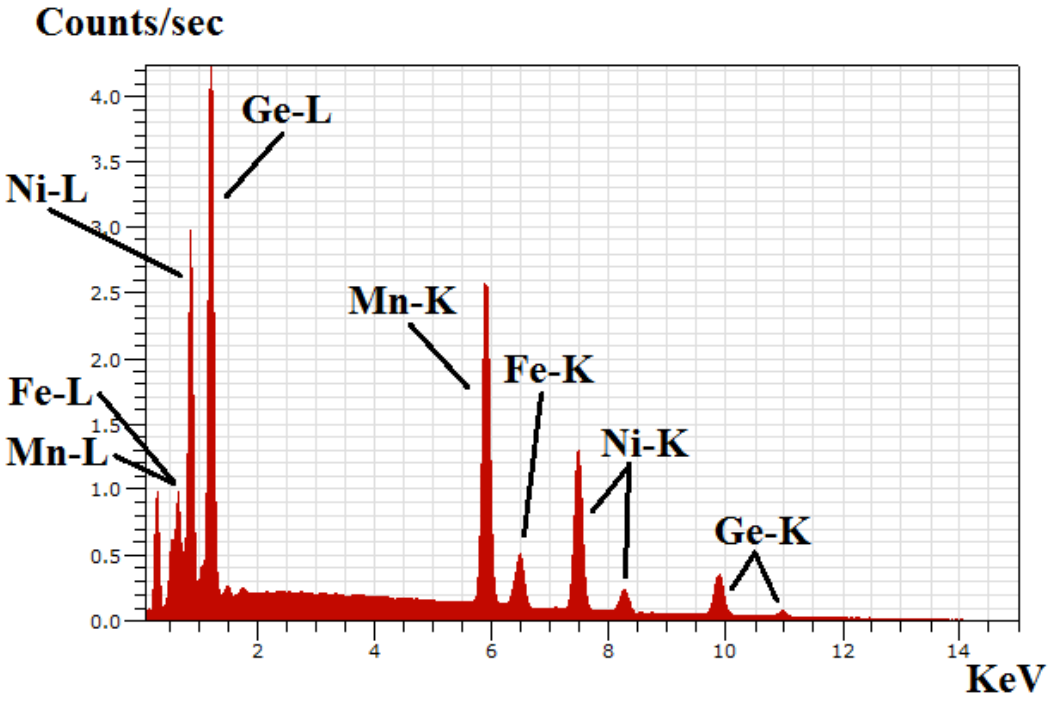

Figure 4.15: *Detected X-rays emitted of the sample surface. Photon energies peaks represent the different elements from the K and L series. The intensities indicate the amount of each element in analyzed region.*

Two, relative flat surface areas shown by figure 4.14 were chosen for further elemental content determination. Table 4.4 shows the elemental content with an estimated error value. Within point one the Fe-substitution on the Mn-site is 5.3 percent, quite close to the $Mn_{0.95}Fe_{0.05}NiGe$ synthetization goal. The second point appears to have a 2.6 percent Fe-substitution on the Mn-site and 3 percent excess Ge.

Table 4.4: *Elemental content of two selected crystallite surfaces in the $Mn_{0.95}Fe_{0.05}NiGe$ powder. Estimated error values are also listed.*

Element	Elemental content (with error) point one	Elemental content (with error) point two
Nickel	34.02% , (1.0 % error)	31.05%, (2.3 % error)
Germanium	32.01%, (2.1% error)	36.42 %, (2.3% error)
Manganese	32.14%, (0.8% error)	31.68%, (0.8% error)
Iron	1.83%, (0.1% error)	0.85%, (0.0% error)

4.5.2 $Mn_{0.95}Fe_{0.05}NiGe$ crystallite surface analysis

For further EDS analysis, single crystallites were analyzed. Crystallite surface regions appearing relative flat were chosen and analyzed with an 4000x picture magnification. Figure 4.16 shows the flat surface of a $Mn_{0.95}Fe_{0.05}NiGe$ crystallite. Elemental composition seems quite well distributed.

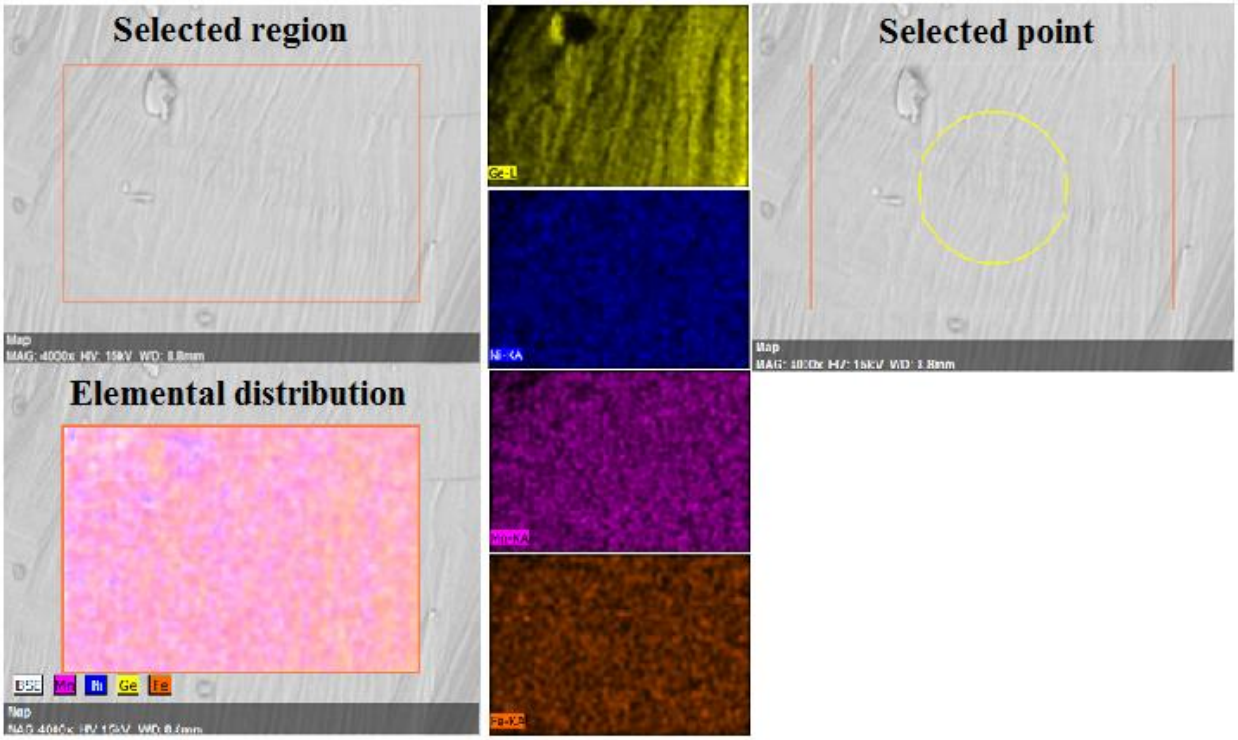

Figure 4.16: *One flat region of a $Mn_{0.95}Fe_{0.05}NiGe$ crystallite. The orange, purple, blue and yellow pictures represent the Fe, Mn, Ni and Ge content of the crystallite surface. Bright spots indicate high elemental content and dark spots indicate low elemental content. The selected point is further analyzed for accurate elemental content determination. The picture was taken with a magnification factor of 4000.*

Table 4.5 shows the elemental content of the selected point in figure 4.16. The Fe substitution on Mn is 5.6 percent. This value is more reliable than for the overview analysis, as there are less disturbance form rough surfaces. Also, as the magnification is amplified by 10, there will be more data points per surface area which gives a higher resolution on the elemental analysis.

Table 4.5: *Elemental content of one selected point at the* $Mn_{0.95}Fe_{0.05}NiGe$ *crystallite surface. Estimated error values are also listed.*

Element	Elemental content (with error) selected point
Nickel	31.30% , (0.9 % error)
Germanium	33.99%, (2.1% error)
Manganese	32.73%, (0.8% error)
Iron	1.97%, (0.1% error)

4.5.3 $Mn_{0.85}Fe_{0.15}NiGe$ crystallite surface analysis

Figure 4.17 shows one flat region of a $Mn_{0.85}Fe_{0.15}NiGe$ crystallite. Just as for the $Mn_{0.95}Fe_{0.05}NiGe$ sample, a crystallite was analyzed with an 4000x picture magnification. One can see that the Fe, Mn and Ni elements are pretty well distributed for the selected region. Some areas for the Ge element are underrepresented, which could indicate some inhomogeneties in the sample.

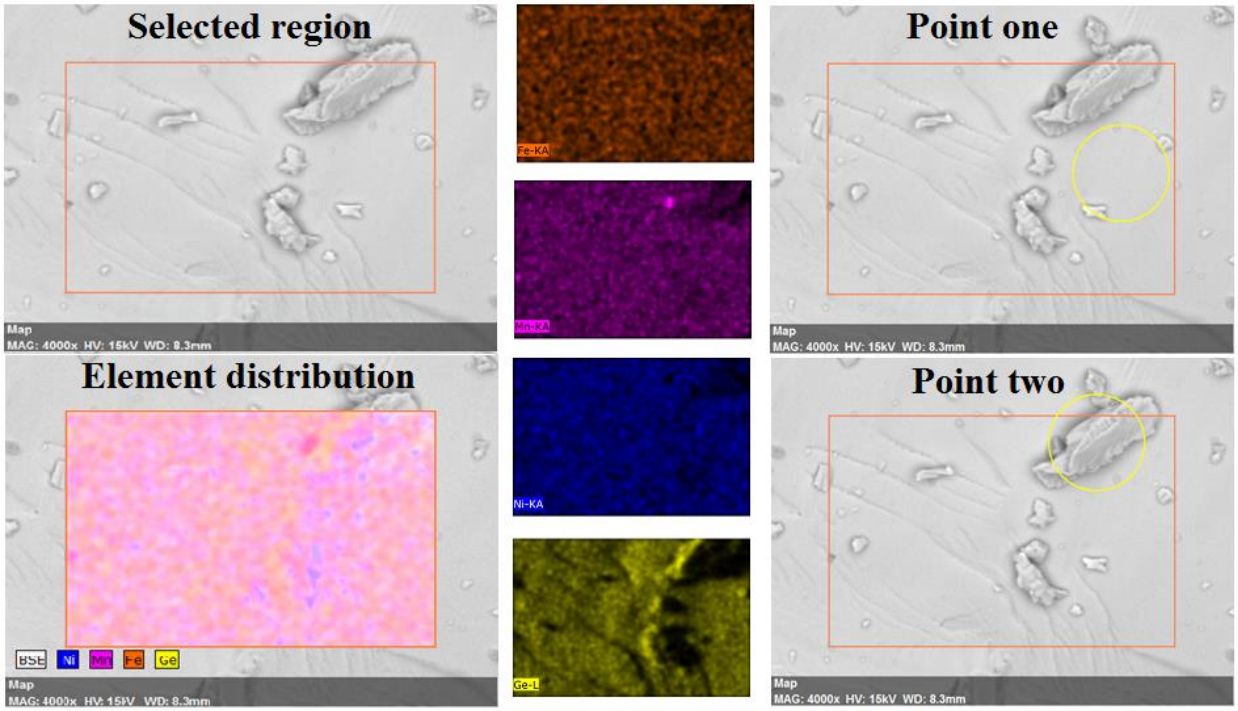

Figure 4.17: *One flat region of a $Mn_{0.85}Fe_{0.15}NiGe$ crystallite. The orange, purple, blue and yellow pictures represent the Fe, Mn, Ni and Ge content of the crystallite surface. Bright spots indicate high elemental content and dark spots indicate low elemental content. The two selected points are further analyzed for accurate elemental content determination. The picture was taken with a magnification factor of 4000.*

The elemental content of the two selected points in figure 4.17 is shown in table 4.6. Within point one the Fe-substitution on Mn is 14.7 percent, quite close to the $Mn_{0.85}Fe_{0.15}NiGe$ synthetization goal. The second point appears to contain some oxygen, but the iron content is pretty close to the value of point one.

Table 4.6: *The elemental content at two points of a $Mn_{0.85}Fe_{0.15}NiGe$ crystallite surface. Estimated error values are also listed.*

Element	Elemental content (with error) point one	Elemental content (with error) point two
Nickel	33.30% , (1.0 % error)	33.57%, (1.1 % error)
Germanium	33.16%, (2.1% error)	27.99 %, (2.0% error)
Manganese	28.62%, (0.7% error)	27.03%, (0.8% error)
Iron	4.92%, (0.1% error)	5.15%, (0.2% error)
Oxygen	-	6.26%, (0.4% error)

A second region of the $Mn_{0.85}Fe_{0.15}NiGe$ sample was additionally analyzed. Figure 4.18 shows a second chosen region of one $Mn_{0.85}Fe_{0.15}NiGe$ crystallite. Apart from some areas with high Mn-content and some areas with absence of Ge, the elemental content seems relatively well distributed. There are some regions where no or little content is shown. These appear to be the same areas for all the elements and are probably due to an uneven crystallite surface.

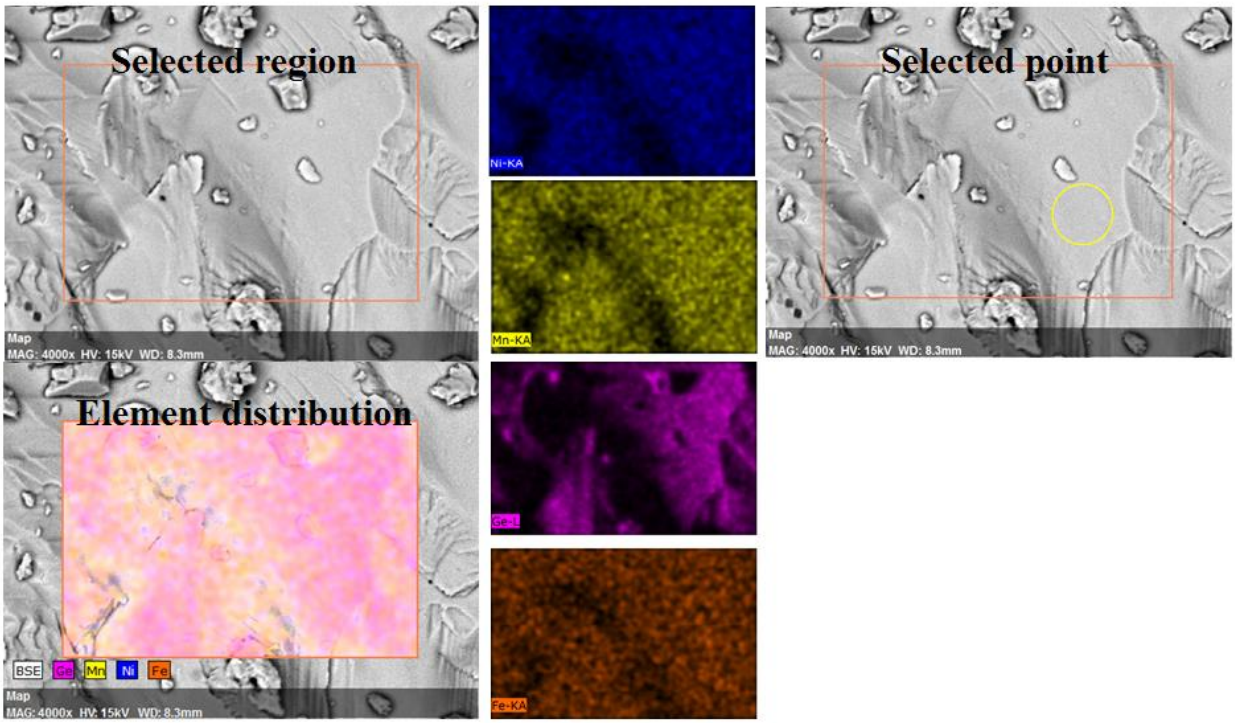

Figure 4.18: *A second, flat region of a $Mn_{0.85}Fe_{0.15}NiGe$ crystallite. The orange, purple, blue and yellow pictures represent the Fe, Ge, Ni and Mn content of the crystallite surface. Bright spots indicate high elemental content and dark spots indicate low elemental content. One selected point is further analyzed for accurate elemental content determination. The picture was taken with a magnification factor of 4000.*

The elemental content of the selected point in figure 4.18 is shown in table 4.7. The Fe-substitution on Mn is 13.7 percent.

Table 4.7: *Elemental content of one selected point at the $Mn_{0.85}Fe_{0.15}NiGe$ crystallite surface. Estimated error values are also listed.*

Element	Elemental content (with error) selected point
Nickel	31.23%, (0.9% error)
Germanium	34.57% , (2.1 % error)
Manganese	29.53%, (0.7% error)
Iron	4.67%, (0.1% error)

For the chosen points on the flat $Mn_{0.95}Fe_{0.05}NiGe$ and $Mn_{0.85}Fe_{0.15}NiGe$ crystallite surfaces, it appears the elemental distributions are quite homogenous. A pattern of small Mn buildup areas and Ge absence areas is noticed. With a 4000x magnification, and part from the oxidized region, the largest deviation between calculated and measured values of Fe-substitution was 1.3 percent. The average offset of the estimated Fe-Mn elemental composition is 0.73 percent

4.6 Magnetic measurements

4.6.1 Temperature dependent magnetization

Figure 4.19 and 4.20 shows the temperature dependent magnetization of the $Mn_{0.85}Fe_{0.15}NiGe$ and $MnNi_{0.85}Fe_{0.15}Ge$ samples. The M(T) data was measured in a constant magnetic field of 0.1 tesla. The $Mn_{0.85}Fe_{0.15}NiGe$ sample shows a sharp magnetic transition from the PM to FM state with clear hysteresis. The PM-FM transition occurs in the same temperature region as the structural transition indicated by the DSC measurements (see figure 4.3). This confirms an established MST from the PM austenite phase to the FM martensite phase. As there is no hysteresis involved in a SOPT, this is FOPT which also implies a magnetostructural coupling. In the temperature region below 160 K there is a missorientation of the magnetic moments, resulting in an antiferromagnetic ordering. This is surprising as Fe-substitution has been reported to induce ferromagnetism in the antiferromagnetic MnNiGe alloy. As the interatomic distance between Mn-magnetic moments are reduced below 2.29 Å, the material orders antiferromagneticly [S. Kumar Pal, personal reference]. This could be the situation as the temperature is reduced below 160 K. Below 125 K, the material reorders in a new antiferromagnetic state.

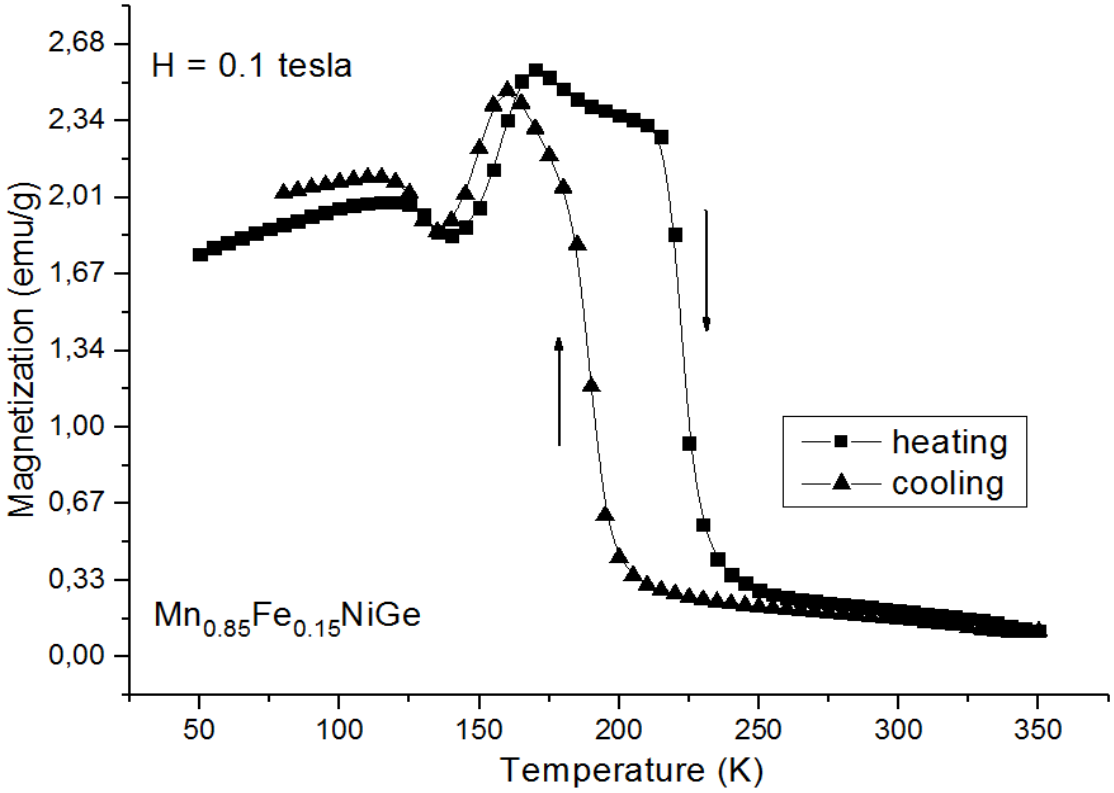

Figure 4.19: *Magnetization (emu/g) of the $Mn_{0.85}Fe_{0.15}NiGe$ sample as a function of themperature. The measurement is performed with a constant magnetic field of 0.1 tesla.*

The $MnNi_{0.85}Fe_{0.15}Ge$ sample shows a steep magnetization initiated at 325 K upon cooling. Along with hysteresis, this is typical behavior of a first order PM-FM magnetostructural coupling. Just at for the $Mn_{0.85}Fe_{0.15}NiGe$ sample, the PM-FM transition occurs in the same temperature region as the structural transition indicated by the DSC measurements (see figure 4.4). In this case the transition does not seem to be perfectly coupled as the initiation of the transition (upon cooling) is steeper than the rest. This could be a result of the structural transition finishing at around 300 K, while the magnetic transition continues below 300 K. Below 275 K the magnetic ordering does not change much until the sample cooled below 190 K. At this point the interatomic distances change, introducing a new magnetic ordering.

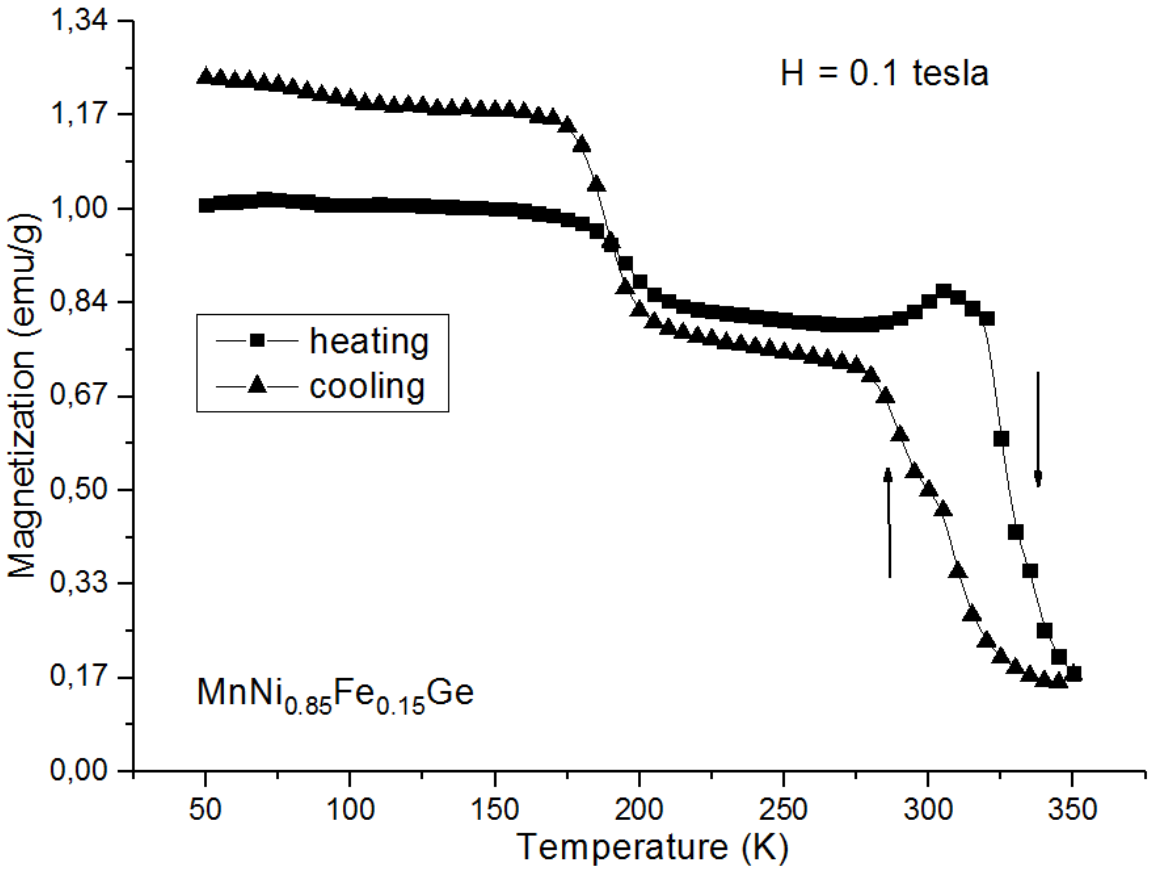

Figure 4.20: *Magnetization (emu/g) of the $MnNi_{0.85}Fe_{0.15}Ge$ sample as a function of temperature. The measurement is performed with a constant magnetic field of 0.1 tesla.*

4.6.2 Field dependent magnetization

For entropy change determination (ΔS_m), M(H) measurement was performed on the $Mn_{0.85}Fe_{0.15}NiGe$ sample. Figure 4.21 shows magnetic isotherms across MST temperature span indicated by figure 4.19. At 220 K, the alloy indicates a typical, almost linear PM magnetization. As the sample temperature is reduced, a steeper magnetization slope is observed. This could be the PM-FM transition. As the isotherms are slightly S-shaped, there could be some additional magnetic transition occurring during the magnetization, like a metamagnetic transitioin [10].

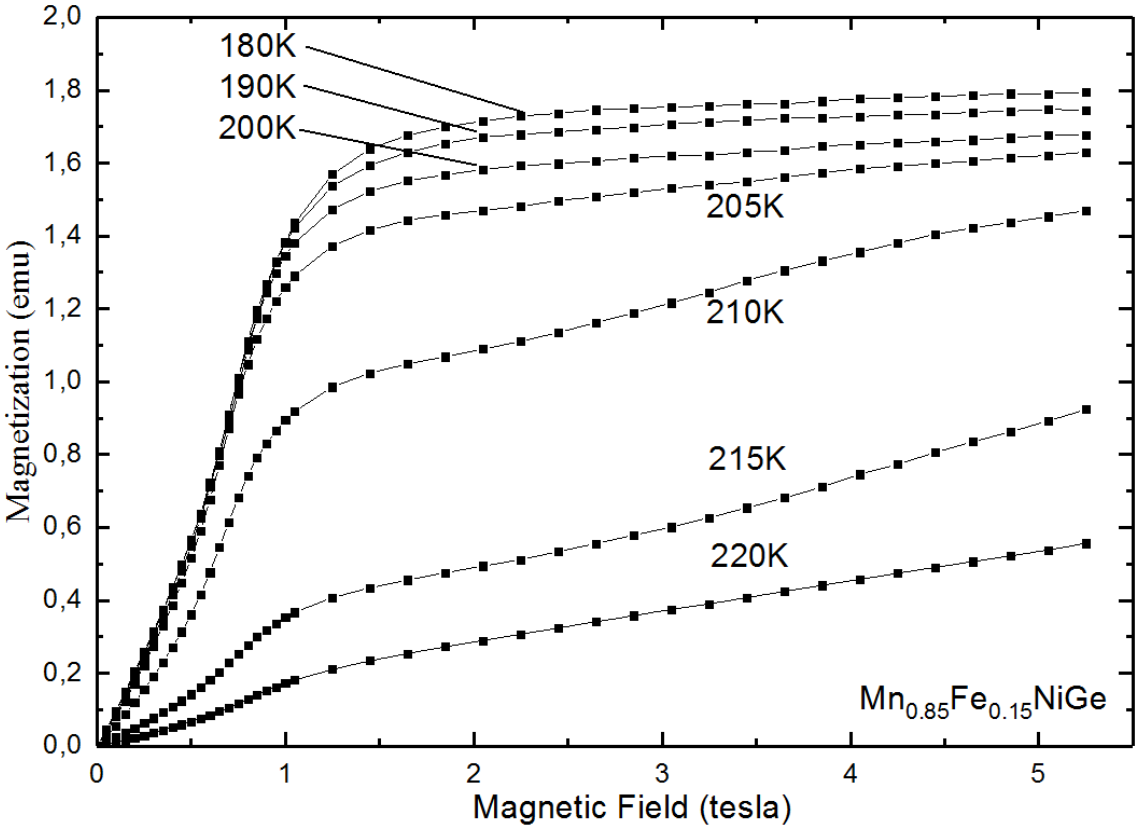

Figure 4.21: *Isotherm magnetization (emu) of the $Mn_{0.85}Fe_{0.15}NiGe$ sample with temperatures chosen according to the MST indicated by figure 4.19. 0.0299 grams of sample were measured.*

4.6.3 Calculated entropy change

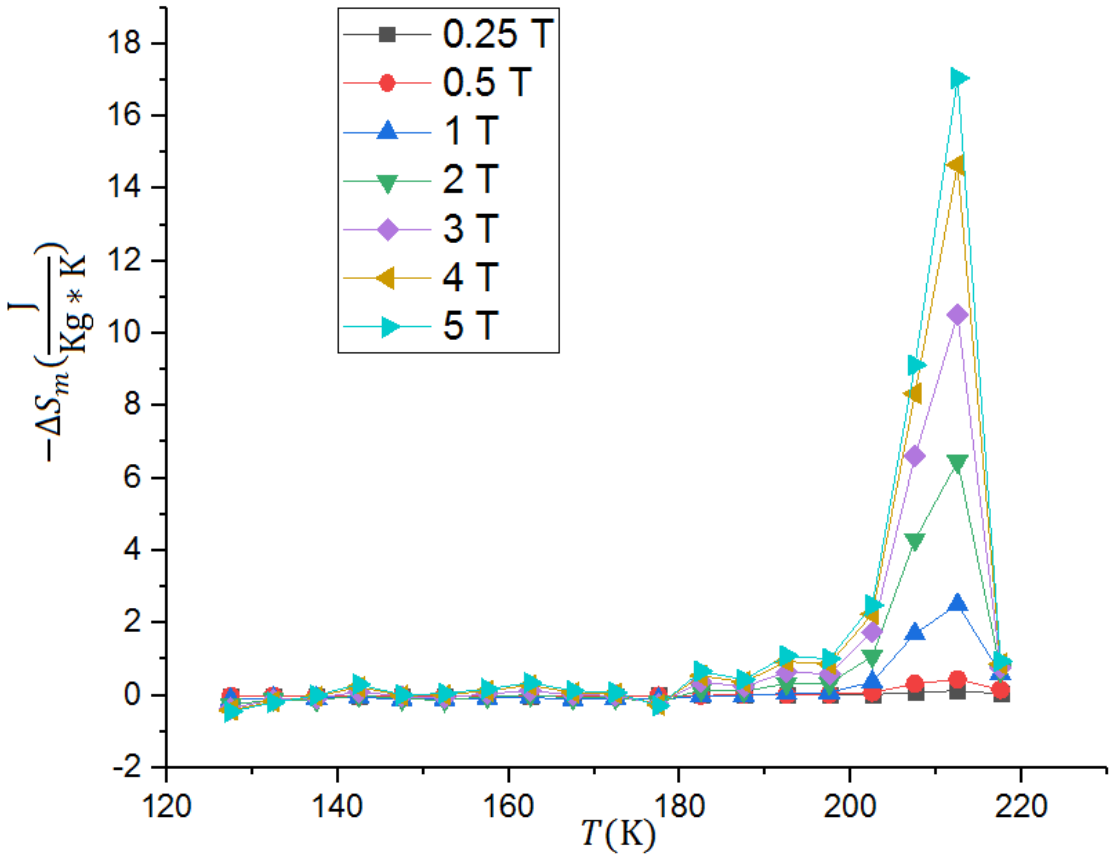

Figure 4.22: *The calculated entropy change of the $Mn_{0.85}Fe_{0.15}NiGe$ sample based on the magnetic isotherms across the MST shown by figure 4.21.*

Figure 4.22 shows the maximum negative entropy change $-\Delta S_m$ at different sample temperatures by appliance of variated magnetic fields. ΔS_m were calculated using the Maxwell equation (2.18) based on the magnetic isotherms across the MST (figure 4.21). A MCE of 6.46 $\frac{J}{Kg*K}$ and 17.06 $\frac{J}{Kg*K}$ is observed at $\Delta H = 2$ T and $\Delta H = 5$ T during the MST. For additional ΔS_m values see appendix C. Due to a limited amount of time, some data points (above 220 K) are missing in order to get a complete description of the magnetostructural ΔS_m values.

Chapter 5

Conclusion

The EDS elemental composition analysis indicates an average offset of 0.73 percent from the desired Fe-Mn composition ratio. From the neutron diffraction experiment, a refined Fe-Mn occupancy deviating 0.9 percent from the estimated value was determined. Although analysis was only preformed on a few selected samples, this gives an indication of the achieved elemental composition accuracy of all the compounds. The sample synthesis process appears to have been quite successful.

The $Mn_{1-x}Fe_xNiGe$ samples form an orthorhombic crystal structure for Fe-substitutions $x < 0.10$. With $x \geq 10$, the compound forms a hexagonal crystal structure with a unit cell volume reduction of approximately 71 $Å^3$. The same situation occurs for the $MnNi_{1-x}Fe_xGe$, compound, but a higher Fe-substitution $(x \geq 0.15)$ is needed to trigger the structural transition. As indicated by the morphology, volume change upon a martensitic transition causes cracking of the crystallites. This could cause a wearing out effect of the material, after a long cyclic lifetime as a magnetic refrigerant. As the powder becomes more granular, the MCE of the material could change.

DSC heat flow signals determine the structural martensitic transition-temperatures of the $Mn_{1-x}Fe_xNiGe$ and $MnNi_{1-x}Fe_xGe$ compounds and indicate an established MST as sufficient iron is introduced. The MST is confirmed by determination of a first order PM-FM magnetic transition in approximately the same temperature region as the martensitic transition. The magnetic measurements were only performed for two samples, but gives reason to believe a MST is established in all the samples showing a single transition peak in the DSC graphs. Fe-substitution appears to reduce the MST significantly as higher iron content is introduced. This makes the MST tunable towards RT.

With sufficient Fe-substitution, the compounds exist in a high temperature austenite (hexagonal, $P\ 6_3/mmc$) PM state and a low temperature FM martensite (orthorhombic, $P\ nma$) state. However, the measured compounds show a misorientantion of magnetic moments and additional magnetic transitions occurring below the MST temperature.

For a selected sample, an entropy change of $6.5\ \frac{\mathrm{J}}{\mathrm{Kg}*\mathrm{K}}$ upon application of a two tesla magnetic field is determined. For comparison, the benchmark Gd has an entropy change of $6.2\ \frac{\mathrm{J}}{\mathrm{Kg}*\mathrm{K}}$ upon a two tesla field. For this sample ($\mathrm{Mn}_{0.85}\mathrm{Fe}_{0.15}\mathrm{NiGe}$), the maximum entropy change (ΔS_m) during the MST occurs at approximately 210 K. The sampe transition-temperature can be tuned towards RT by a reduction of approximate 5 percent Fe-substitution on the Mn site. Both the magnetic and structural transition indicated hysteresis, which is associated with effect loss in a magnetic heat pump device, but the hysteresis appears to be significantly lower as the transition occurs around RT.

For further cooling power determination of the MCE, additional heat capacity data is needed. This requires DSC scans with a magnetic field source, or direct measurements of the MCE in a MCM.

References

[1] K.A. Gschneidner Jr, V.K Pecharsky 25 January 2008 Thirty years of near room temperature magnetic cooling: Where we are today and future prospects International Journal of Refrigeration Volume 31

[2] P. Dutta, S.Pramanic, S. Majumdar, D. Das, S.Chatterjee 28. July 2015 Magnetofunctional behavior of Fe-doped MnNiGe magnetic equiatomic compound Journal of Magnetism and Magnetic Materials Volume 395

[3] R. Ross 02.08.17 Who Invented the Refrigerator? http://www.livescience.com/57797-refrigerator-history.html Accessed: 25. April 2017

[4] U.S Department of Energy Updated December 2009 Refrigeration Market Profile http://apps1.eere.energy.gov/states/pdfs/ref_market_profile.pdf Accessed: 25. April 2017

[5] U.S Department of Energy AIR CONDITIONING https://energy.gov/energysaver/air-conditioning Accessed: 25. April 2017

[6] The National Academies of Sicence, Engineering and Medicine. Refrigeration http://needtoknow.nas.edu/energy/energy-efficiency/refrigeration/ Accessed: 25. April 2017

[7] The National Academies of Sicence, Engineering and Medicine. Heating and Cooling http://needtoknow.nas.edu/energy/energy-efficiency/heating-cooling/ Accessed: 25. April 2017

[8] J. Lyubina 5 January 2017 Magnetocaloric materials for energy efficient cooling Journal of Physics D:Applied physics volume 50

[9] V. Belusa 01.13.15 Prototpye of Magnetocaloric Wine Cool http://www.chemistryviews.org/details/news/7261611/Prototype_of_Magnetocaloric_Wine_Cooler.html Accessed: 04.26.17

[10] A. Sun, J. Liu, C. Jiang, E. Liu, G. Wu 29. May 2015 First-order magnetic and mangetostructural transitions in the magnetocaloric compound $MnNi_{0.73}Fe_{0.27}Ge$ Physica B Volume 474

[11] W. Borchardt-Ott 2011 Crystallography An Introduction Third Edition Springer Berlin Heidelberg

[12] Lecture by Dr. C. Lind University of Toledo https://www.youtube.com/watch?v=oj4QJ-1lxgU Watched 08.03.2017

[13] S. A. Speakman, Ph.D. Basics of X-Ray Powder Diffraction Massachusetts Institute of Technology, MIT http://prism.mit.edu/xray/oldsite/Basics%20of%20X-Ray%20Powder%20Diffraction.pdf Accessed: 10. Mars 2017

[14] J. S. Lilley and Sons 2001 Nuclear Physics – Principles and Applications Department of Physics and Astronomy, The university of Manchester Baffins Lane, Chester, West Sussex, England

[15] P. A. Tipler, G Mosca 2008 Physics For Scinetists and Engineers Sixth Edition W.H Freeman and Company 41. Madison Avenue New York

[16] P.Papon, J. Leblond, P.H.E Meijer 2002 The Physics of Phase Transitions –Concepts and Applications Springer Berlin Heidelberg

[17] R. Szymczak, R Kolano, A. Kolano-Burian, V.P. Dyakonov, H. Szymczak 2010 Giant magnetocaloric Effect in Magnatites Acta Physica Polonica A Volume 117

[18] M. H. Sørby, 16. February 2010 Powder Neutron Diffraction – an introduction Institute for Energy Technology

[19] A seminar given by Dr. W. Woo. 23. April 2014 An introduction to neutron diffraction in steel research [https://www.youtube.com/watch?v=ysd6CrH-UBM] watched: 28. February 2017

[20] J. S. Lilley and Sons 2001 Nuclear Physics – Principles and Applications Department of Physics and Astronomy, The university of Manchester Baffins Lane, Chester, West Sussex, England Page 218

[21] S.Y Dan'Kov, A.M Tishin, V.K Pecharsky, K.A Gschneidner 1998 Phys. Rev. BVolume 57 (3478-3490)

[22] V.K. Pecharsky, K.A. Gschneidner, 1997 Phys. Rev. Lett. Volume 78 (4494-4497)

[23] A.O. Pecharsky, K.A. Gschneidner, V.K. Pecharsky 2003 J. Appl. Phys Volume 93 (4722-4728)

[24] A.O. Pecharsky, K.A. Gschneidner, V.K. Pecharsky 2003 J. Appl. Phys. Volume 93 (4722-4728)

[25] F.X. Hu, B.G. Shen, J.R. Sun, X.X. Zhang, 2000 Chin. Phys. Volume 9 (550-553)

[26] A. Fujita, S. Fujieda, K. Fukamichi, H. Mitamura, T. Goto 2002 Phys. Rev. B Volume 65

[27] F.X. Hu, B.G. Shen, J.R. Sun, Z.H. Cheng 2001 Phys. Rev. B Volume 64

[28] J.R. Proveti, E.C. Passamani, C. Larica, A.M. Gomes, A.Y. Takeuchi, A. Massioli, 2005 J. Phys. D-Appl. Phys. Volume 38 (1531-1539)

[29] J. Lyubina, R. Schafer, N. Martin, L. Schultz, O. Gutfleisch 2010 Adv. Mater. Volume 22 (3735-+)

[30] A. Reichmuth March 2000 Estimating Weighing Uncertainty From Balance Data Sheet Specifications METTLER TOLEDO

[31] K. Mohomed, Ph. D Differential Scanning Calorimetry (DSC) TA Instruments

[32] J. Bobroff, F. Bouquet, N. Brun, C. Colliex, F. Livolant F. Restagno 01. June 2016 Video: Scanning electron microscope (SEM) DAFOX http://toutestquantique.fr/en/scanning-electron/ watched: 20. Mars 2017

[33] S. Swapp Scanning Electron Microscopy (SEM) University of Wyoming http://serc.carleton.edu/research_education/geochemsheets/techniques/SEM.html Accessed 20. Mars 2017

[34] E. Clementyve 2004 Mangetic Susceptibility: Basic principles and features of the PPMS

[35] CARBOLITE GERO 2017 http://www.carbolite-gero.com/products/chamber-furnaces/laboratory-furnaces/cwf-standard-chamber-furnaces/ Accessed: 14. Mars 2017

[36] PIKE Technologies 2017 https://www.piketech.com/PM-CrushIR-Digital-Hydraulic-Press.html Accessed: 15. Mars 2017

Appendix A:

Calculated and weighted sample batches

Table A.1: *Calculated and weighted sample batches for the $Mn_{1-x}Fe_xNiGe$ compounds with four percent excess of Mn to compensate for evaporation. The calculated offset values are also listed.*

Doping on manganese:							
Iron doping levels:		3 %	5 %	7 %	10 %	15 %	25 %
Elements	***Molecular weight***	**Fraction**	**Fraction**	**Fraction**	**Fraction**	**Fraction**	**Fraction**
Iron	55.845	0.03	0.05	0.07	0.1	0.15	0.25
Manganese	54.938	1.01	0.99	0.97	0.94	0.89	0.79
Nickel	58.6934	1	1	1	1	1	1
Germanium	72.63	1	1	1	1	1	1

Sample molecular weight:	188.48613	188.50427	188.52241	188.54962	188.59497	188.68567

Batchsize:	2g						
Amount of moles per sample:		0.0106109	0.0106098	0.0106088	0.0106073	0.0106047	0.0105996

Calculated weight (g)	Iron	0.0178	0.0296	0.0415	0.0592	0.0888	0.1480
	Manganese	0.5888	0.5771	0.5653	0.5478	0.5185	0.4600
	Nickel	0.6228	0.6227	0.6227	0.6226	0.6224	0.6221
	Germanium	0.7707	0.7706	0.7705	0.7704	0.7702	0.7699
Measured weight (g)	Iron	0.0177	0.0296	0.0414	0.0586	0.0898	0.1478
	Manganese	0.5877	0.5760	0.5642	0.5482	0.5175	0.4642
	Nickel	0.6220	0.6224	0.6210	0.6241	0.6210	0.6231
	Germanium	0.7723	0.7703	0.7698	0.7764	0.7695	0.7654

Offset (g)	Iron	-0.0001	0.0000	-0.0001	-0.0006	0.0010	-0.0002
	Manganese	-0.0011	-0.0011	-0.0011	0.0004	-0.0010	0.0042
	Nickel	-0.0008	-0.0003	-0.0017	0.0015	-0.0014	0.0010
	Germanium	0.0016	-0.0003	-0.0007	0.0060	-0.0007	-0.0045

Table A.2: *Calculated and weighted sample batches for the $MnNi_{1-x}Fe_xGe$ compounds with four percent excess of Mn to compensate for evaporation. The calculated offset values are also listed.*

Doping on nickel					
Iron doping levels on nickel:		5 %	10 %	15 %	25 %
Elements	**Molecular weight**	**Fraction**	**Fraction**	**Fraction**	**Fraction**
Iron	55.845	0.05	0.1	0.15	0.25
Manganese	54.938	1.04	1.04	1.04	1.04
Nickel	58.6934	0.95	0.9	0.85	0.75
Germanium	72.63	1	1	1	1

Sample molecular weight:	188.3165	188.17408	188.03166	187.74682

Batchsize:	2g				
Amount of moles per samle:		0.010620418	0.010628456	0.01063651	0.0106526
Calculated weight per sample (g)	Iron	0.0297	0.0594	0.0891	0.1487
	Manganese	0.6068	0.6073	0.6077	0.6086
	Nickel	0.5922	0.5614	0.5306	0.4689
	Germanium	0.7714	0.7719	0.7725	0.7737
Measured weight per sample (g)	Iron	0.0298	0.0544	0.0899	0.1473
	Manganese	0.6048	0.6016	0.6079	0.5996
	Nickel	0.5934	0.5655	0.5309	0.4693
	Germanium	0.7705	0.7686	0.7716	0.7751
Offset (g)	Iron	0.0001	-0.0050	0.0008	-0.0014
	Manganese	-0.0020	-0.0057	0.0002	-0.0090
	Nickel	0.0012	0.0041	0.0003	0.0004
	Germanium	-0.0009	-0.0033	-0.0009	0.0014

Table A.3: *Calculated and weighted sample batch for the three gram $Mn_{0.85}Fe_{0.15}NiGe$ compound with four percent excess of Mn to compensate for evaporation. The calculated offset values are also listed.*

Neutron experiment:		
Calculated weight per sample (g)	**Iron**	0.1332
	Manganese	0.7778
	Nickel	0.9336
	Germanium	1.1553
Batchsize:	3	
Sample molecular weight	188.59497	
Mol/sample	0.01590711	

Measured weight (g)	**Iron**	0.1347
	Manganese	0.7791
	Nickel	0.9354
	Germanium	1.1555
Offset (g)	**Iron**	0.0015
	Manganese	0.0013
	Nickel	0.0018
	Germanium	0.0002

Appendix B:

Lattice parameters with standard deviation

Table B.1: *The $Mn_{1-x}Fe_xNiGe$ refined lattice parameters with additional phases. The a parameter indicate a reduction trend. Lattice parameters b and c indicates no trend.*

Fe substitution on Mn-side						
Doping	**Main phase**			**Additional phase**		
	a	**b**	**c**	a	**b**	**c**
X=0	6.0399	3.7558	7.0912	4.082254	4-082254	5.394991
Std.	0.0017	0.0009	0.0018	0.079335	0.079335	0.115669
X=3	6.0275	3.7521	7.0837			
Std.	0.0024	0.0014	0.0027			
X=5	6.0220	3.7533	7.0920	-	-	-
Std.	0.0014	0.0009	0.0016	-	-	-
X=7	6.0197	3.7512	7.0894			
Std.	0.0015	0.0009	0.0017			
X=10	4.0879	4.0879	5.3795			
Std.	0.0005	0.0052	0.0007			
X=15	4.0877	4.0877	5.3549			
Std.	0.0005	0.0005	0.0007			
X=25	4.0855	4.0855	5.3216			
Std.	0.0007	0.0007	0.0011			

Table B.2: *The $MnNi_{1-x}Fe_xGe$ refined lattice parameters with additional phases. Lattice parameter a indicate a trend of decreasing and c indicates a trend of increasing. Lattice parameters b indicates no trend.*

Fe substitution on Ni-side									
Doping	**Main phase**			**Additional phase**			**Additional phase**		
	a	**b**	**c**	**a**	**b**	**c**	**a**	**b**	**c**
X=0	6.0399	3.7558	7.0912						
Std.	0.0017	0.0009	0.0018						
X=5	6.0332	3.7564	7.0938	4.058	4.058	5.038			
Std.	0.0023	0.0014	0.0026	-	-	-			
X=10	6.0329	3.7648	7.0948						
Std.	0.0020	0.0012	0.0022						
X=15	6.0306	3.7742	7.1047	4.0941	4.0941	5.0346	4.0968	4.0968	5.3937
Std.	0.0025	0.0015	0.0029	0.0039	0.0039	0.0053	0.0019	0.1192	0.0028
X=25	4.0937	4.0937	5.3758						
Std.	0.0005	0.0005	0.0007						

Appendix C

Calculated entropy change of $Mn_{0.85}Fe_{0.15}NiGe$ sample

Table C.1: *The calculated negative entropy change $-\Delta S_m$ at different sample temperatures by appliance of variated magnetic fields.*

	Negative delta S (J/(Kg*K))						
Temp	tesal (T)						
	0.25 (T)	0.5 (T)	1 (T)	2 (T)	3 (T)	4 (T)	5 (T)
217.5	0.04725	0.15702	0.604949	0.684117	0.76878	0.87084	0.9451
212.5	0.12452	0.447	2.517835	6.46258	10.5173	14.6621	17.0592
207.5	0.09245	0.3194	1.706701	4.307642	6.61261	8.34178	9.12947
202.5	0.02661	0.07916	0.36873	1.08569	1.74847	2.25065	2.49514
197.5	0.01208	0.03076	0.087974	0.337823	0.59933	0.8693	1.01297
192.5	0.00637	0.01264	0.05649	0.327839	0.64313	0.93601	1.09664
187.5	0.00596	0.01241	-5.2E-05	0.114572	0.23914	0.36926	0.4377
182.5	0.00251	0.00112	-0.01044	0.159585	0.3745	0.54247	0.66585
177.5	0.00081	0.00794	-0.11885	-0.19071	0.22968	0.26071	0.29022
172.5	0.00276	0.01243	-0.08355	-0.0613	0.00195	0.05426	0.08119
167.5	0.00269	0.01183	-0.10578	-0.07168	0.01639	0.08645	0.13577
162.5	0.00606	-0.0113	-0.05935	0.016019	0.13086	0.27903	0.35371
157.5	0.00829	0.01186	-0.06644	-0.02933	0.04217	0.12625	0.18234
152.5	0.01095	0.01619	-0.10555	-0.12709	0.06373	0.01669	0.05701
147.5	0.01089	0.01882	-0.10194	-0.0908	0.02544	0.00458	0.01526
142.5	0.00961	0.01243	-0.0535	0.002549	0.10805	0.23421	0.30835
137.5	0.00714	0.00999	-0.08224	-0.12842	0.08334	0.02814	0.00225
132.5	0.00531	0.01079	-0.09008	-0.11703	-0.1189	0.16724	0.19587
127.5	0.00894	0.01694	-0.11123	-0.26072	0.35276	0.40581	0.45044

Table C.1 shows negative calculated maximum entropy change values ($-\Delta S_{\mathrm{m}}$) of $Mn_{0.85}Fe_{0.15}NiGe$ at different temperatures.

Norges miljø- og biovitenskapelig universitet
Noregs miljø- og biovitskapelege universitet
Norwegian University of Life Sciences

Postboks 5003
NO-1432 Ås
Norway